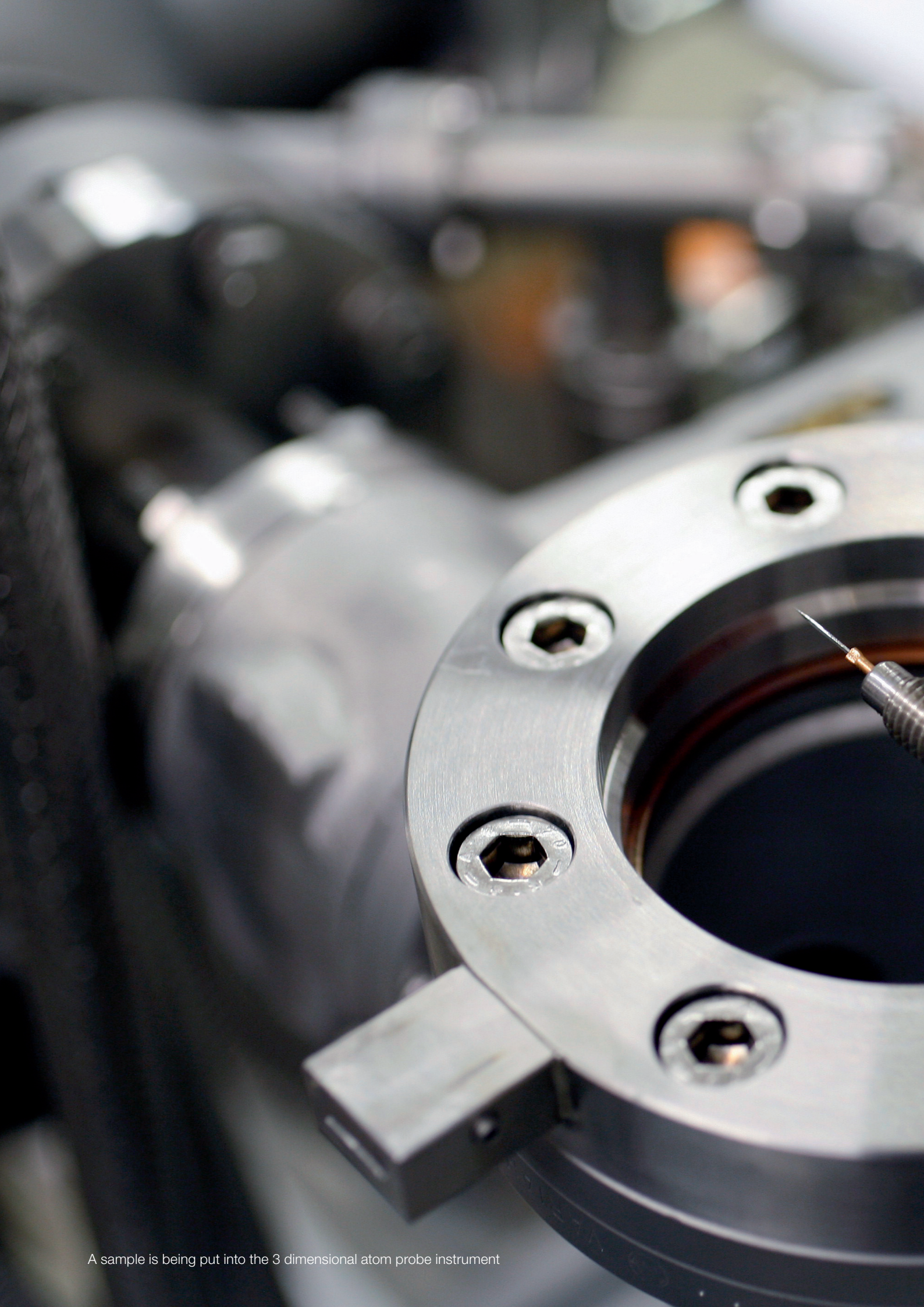

A sample is being put into the 3 dimensional atom probe instrument

Scientific Highlights
Structure Research 2006

BENSC User Service	30
NAA User Service	34
SF1 Methods and Instruments	36
SF2 Magnetism	40
SF3 Materials	44
SF4 Structure and Dynamics	48
SF6 Trace Elements	52
SF7 Nuclear Measurements	54
SFN1 Magnetism and Superconductivity of Quantum Materials	56

(Photo: Bernhard Schurian)

Are cold neutrons cool enough to help us get home faster?

L.P. Aldridge[1] H.N. Bordallo[2], A. Desmedt[3]

■ 1 Materials & Engineering Science ANSTO School of Civil and Environmental Engineering, UNSW, Australia ■ 2 HMI, SF6 ■ 2 Groupe de Spectroscopie Moléculaire, ISM, Université Bordeaux 1, France

Fig. 1: Remedial treatment to plastic cracking in a new bridge deck prior to opening.

In 2005, more than 5 billion tons of concrete were made. Well-made concrete has a long service life, and it should be possible to build structures that are almost maintenance free from it. However, due to poor concrete technology many structures deteriorate. For example, some bridge decks need maintenance after seven years of exposure to salt either from de-icing or marine sources. These repairs can be costly – for example, in the USA, it has been estimated that over a billion dollars need to be spent each year to repair concrete bridge decks.

The key to making durable concrete is to limit the ability of concrete to transport fluids (like water)[1]. Poorly made concrete will have cracks and pores allowing water to travel easily through, while in well made concrete it is more difficult for water to penetrate. Concrete is made from cement paste and a number of inert aggregates and in un-cracked concrete it is the cement paste that will transport the water.

As cement hydrates, sets and hardens, it forms pores which are classified either as “capillary pores”, if the pore diameter is larger than 100Å, or “gel pores” for the smaller pores. When the water content in the paste is such that the water to cement ratio (w/c) is less than, and the paste is properly cured, then the capillary pores become discontinuous. Then it is the gel pores that will limit water transport in concrete.

This joint research between the Hahn-Meitner-Institut (HMI) in Berlin, the IMES Australian Nuclear Science and Technology Organization (ANSTO) and the School of Civil and Environmental Engineering, University of New South Wales in Sydney, Australia combines practical work on large

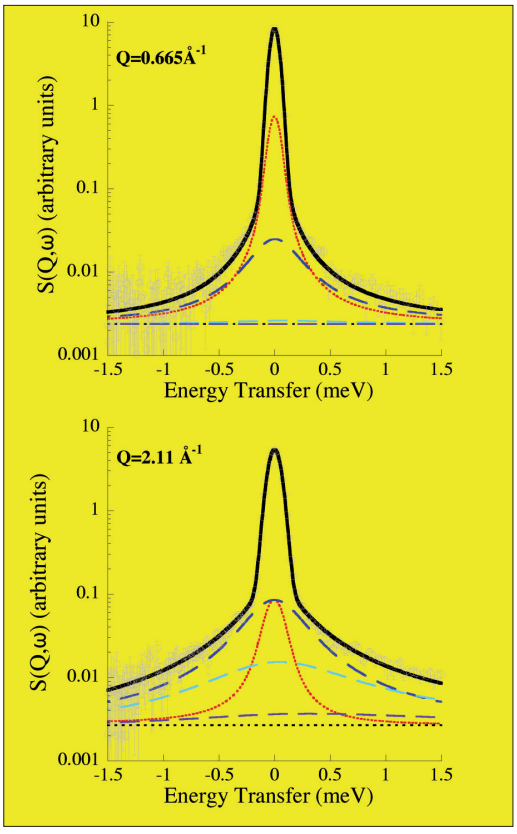

Fig. 2: Examples of experimental spectra (○) at selected Q-values for the cement paste with w/c=0.42, ΔE=98μeV, together with the best fit (solid line) and the quasi-elastic components (dotted lines represents the translational component and the long dashed lines represents the first three terms of the Sears expansion used to describe the rotational motion). The background is also shown (short dashed line).

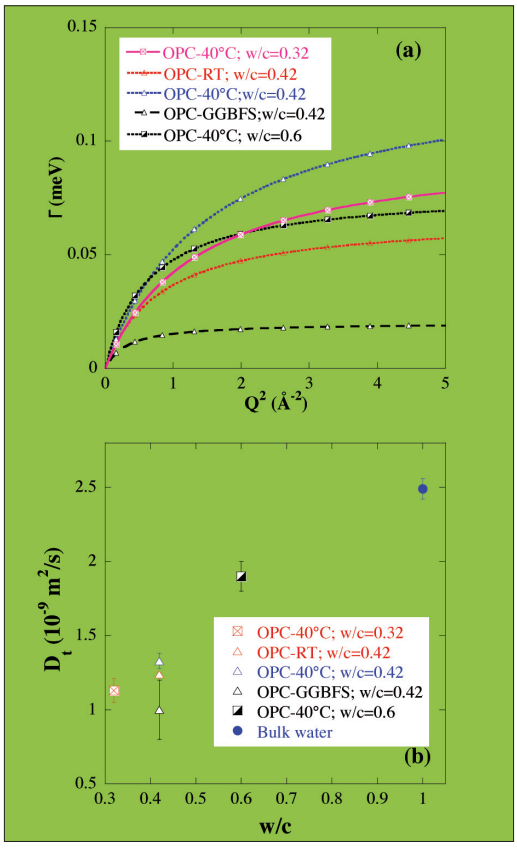

Fig. 3: (a) Line-width (Γ, HWHM) as a function of Q^2 of the quasi-elastic component for water contained in cement pastes, using 5.1 Å neutrons, with $\Delta E = 98$ μeV The solid lines are fit to the data using the model of Singwi and Sjölander.[2,3] (b) Self-diffusion coefficient (D_t) vs w/c content for the different pastes.

concrete blocks with measurements on small samples to determine how water moves in the hardened cement paste.

In complex systems such as hardened cement pastes, it is neither easy nor straightforward to determine the origin of the observed differences in the dynamical behavior of the water molecules. However, quasi-elastic neutron scattering (QENS) has been used to estimate the dynamics of confined and interfacial water. Using HMI's time-of-flight spectrometer NEAT, we have performed a series of QENS experiments to investigate the dynamics of water in the pores within the cement paste. It was possible to measure the diffusion of water in 1 g of paste.

QENS spectra of a number of different cements have been measured and analyzed as outlined in Bordallo et al [4] in terms of rotation and long range translational motion. The quasi elastic widths (Γ) plotted as a function of Q^2 are shown in Figure 3(a). From the slope we calculated the translational diffusion of water while the saturation values at higher Q's gave the rotational values. This approach indicates that at least two diffusion processes occurred. A fast diffusion is most likely attributable to the water confined in the capillary pore structure ($D_t \sim 10^{-9}$ m^2/s) and a slower diffusion is probably due to gel pore water ($D_t \sim 10^{-10}$ m^2/s). In addition from high-resolution backscattering measurements a slower motion was also detected, that could be associated with a long-range translational diffusion [5].

Our work [4] distinguishes between three different types of water confirming the interpretation of previous NMR experiments [6]. Thus QENS is able not only to distinguish between the types of water but it also quantifies the rotation and diffusion of this water. Pastes made under different conditions (i.e. with Ground Granulated Blast Furnace Slag (GGBFS), or different water/cement ratios (w/c) or cured at room temperature (RT) or 40°C) give significantly different diffusivities as shown in Figure 3(b).

The long term aim of the work is to develop tests that show the "fitness for purpose of concrete" within the first week of concrete setting. Such tests can only take place if the role of water in the gel pores is understood. When this is achieved, then "in-situ" tests may be developed to show if the concrete has been properly cured and compacted. Then estimates of the durability of concrete could be made on site during construction. Thus maintenance-free concrete bridge decks could be built and such frequent bridge repairs will no longer be needed. So if cold neutrons are cool enough to measure the slow diffusivity of water in cement paste, tests will be developed so less reconstruction is needed. Perhaps then neutrons will have helped us get home faster from work.

[1] S. Mindess, J.F. Young, D. Darwin, in Concrete - 2nd ed.; Prentice Hall, 2003
[2] K.S. Singwi and A. Sjölander, Phys. Rev., **119**, 863 (1960)
[3] M. Beé, in Quasi-Elastic Neutron Scattering; Adam Hilger, Bristol, Philadelphia, 1988
[4] H.N. Bordallo, L.P. Aldridge and A. Desmedt, J. Phys. Chem. B, **110**, 17966 (2006)
[5] L.P. Aldridge, H.N. Bordallo and A. Desmedt, Physica B, **350**, e565 (2004)
[6] J. Greener, H. Peemoeller, C. Choi, R. Holly, E.J. Reardon, C.M. Hansson and M.M. Pintar, J. Am. Ceram. Soc., **83**, 623 (2000)

Corresponding authors:
L.P. Aldridge
laurie.aldridge@gmail.com
H.N. Bordallo
bordallo@hmi.de

Magnetic excitations in the magnetically ordered phases of PrB_6

K. A. McEwen[1], M. D. Le[1], K. C. Rule[2], J-G. Park[3], S. Lee[3], F. Iga[4]

■ 1 Department of Physics and Astronomy, University College London, UK ■ 2 HMI, SF1
■ 3 Department of Physics, SungKyunKwan University, Suwon, Korea ■ 4 Department of Quantum Matter, Hiroshima University, Japan

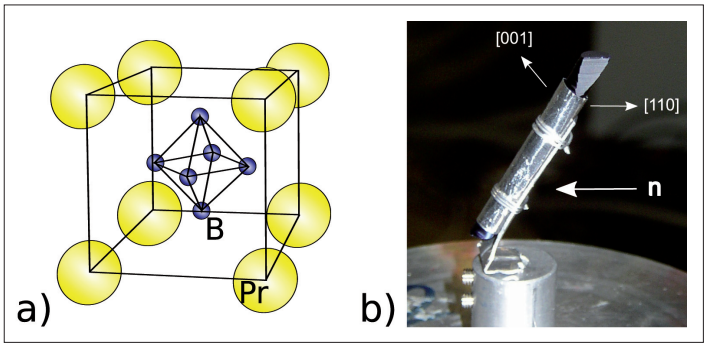

Fig. 1: (a) Crystal structure of PrB_6; (b) The single crystal of PrB_6 as oriented and mounted for the zero field experiments.

The RB_6 family of intermetallic compounds exhibit a particularly interesting range of electrical and magnetic properties, as the number of 4*f* electrons in the rare-earth (R) element increases. At the start of the rare-earth sequence, La has no 4*f* electrons and so is non-magnetic, but displays superconductivity at low temperatures. The single 4*f* electron in CeB_6 is strongly hybridised with the conduction electrons, leading to an enhanced effective mass and showing the characteristic "heavy fermion" behaviour in its electrical resistivity, heat capacity and magnetic susceptibility at low temperatures. CeB_6 does not exhibit ordering of its magnetic dipole moments, but instead the electric quadrupole moments of the 4*f* electrons develop long-range ordering below 3.3K. The various quadrupolar phases of CeB_6 have been extensively studied. However, with two 4*f* electrons, PrB_6 does show long-range ordering of the magnetic dipole moments, as do the remaining members of the RB_6 family (with the exception of divalent EuB_6 and mixed-valent SmB_6).

The crystal structure of PrB_6, like the other RB_6 compounds, is rather straightforward, consisting of a cage of Pr^{3+} ions in a simple cubic structure, with an octahedron of boron atoms within this cage (see Fig. 1a). The aim of our neutron scattering experiments at HMI has been to investigate the magnetic excitations in PrB_6 and hence to determine the magnetic interactions between the Pr ions in this system.

The crystal used for our experiments (shown in Fig. 1b) was grown at Hiroshima University in Japan by means of a floating-zone method. Natural boron comprises an approximately equal mixture of the isotopes ^{10}B and ^{11}B. Since ^{10}B strongly absorbs thermal and cold neutrons, our PrB_6 crystal was prepared using boron enriched to 99% of the non-absorbing ^{11}B isotope.

Earlier neutron diffraction experiments have revealed the magnetic structures of PrB_6. At the lowest temperatures, below 4.2K, the Pr moments orders in the magnetic structure shown in Fig. 2a. This comprises two coexisting chains of antiferromagnetic moments directed at right angles to each other along [110] and $[1\bar{1}0]$ in a so-called *commensurate double-q structure*, with associated wave vectors [¼ ¼ ½] and $[¼\ \bar{¼}\ ½]$. Between 4.2K and 7.0K the system adopts the *incommensurate double-q structure* shown in Fig. 2b, where the periodicity of the magnetic moments is no longer an integer multiple of the lattice periodicity. The application of a magnetic field simplifies the structures considerably. Above a field of 2 tesla, we find the *commensurate single-q* magnetic structure shown in Fig. 2c, with all the magnetic moments perpendicular to the magnetic field direction.

Our inelastic neutron scattering experiments have been carried out using the V2/FLEX triple-axis spectrometer. The Pr^{3+} ions have a total angular momentum J=4: the 9-fold degeneracy of the ground $^3H_4$ multiplet is removed by the cubic crystalline electric field into a singlet, a doublet and two triplet states. The ground state is the Γ_5 triplet with a first excited Γ_3 doublet at 27meV. In the magnetically ordered phases, the Γ_5 triplet is itself split by the molecular (internal) field. Hence the low energy excitations in the ordered phases are expected to be due entirely due to spin waves from this splitting, which is ~1-2meV.

In our experiments we have mapped out the dispersion of these low energy excitations along the principal symmetry directions ([*h h* 1½] and [¼ ¼ l]) around the magnetic Brillouin zone centre at (¼ ¼ 1½). Fig. 3 shows the dispersion along [h h 1½], with a typical scan shown in Fig. 4a.

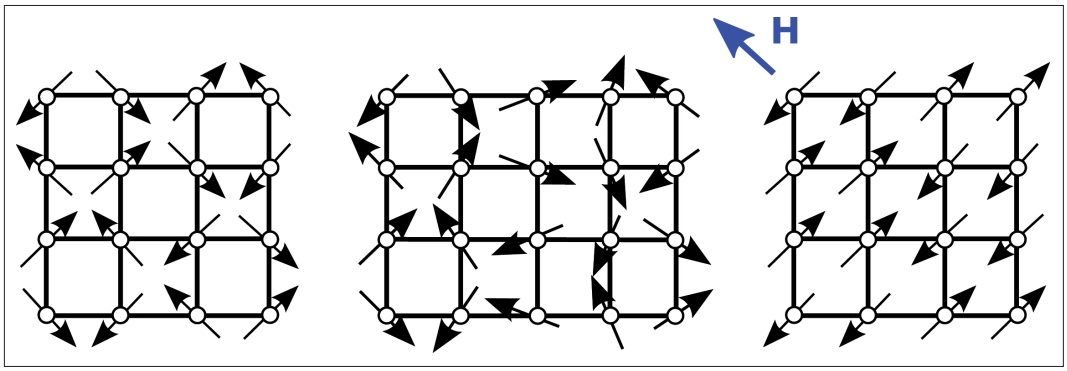

Fig. 2: Magnetic structures of PrB_6; (a) Commensurate double-q structure for T<4.2K; (b) Incommensurate double-q structure for 4.2K<T<7K; (c) Commensurate single-q structure for fields above 2 tesla along the direction shown.

Three modes are clearly observed at the magnetic zone boundary: the two lower energy modes merge near the middle of the zone. Analysis of these results shows that the dominant magnetic interactions are between nearest neighbour Pr ions, but that interactions up to fourth nearest neighbours are required to explain the dispersion relation in zero applied magnetic field.

As discussed above, the application of a magnetic field leads to a dramatic simplification of the magnetic structure. The dispersion of the excitations along [*h h* 1½] becomes significantly greater as can be seen in Fig. 3. Moreover, only a single mode is now observed: Fig. 4b shows that two of the modes seen in Fig. 4a are suppressed by the magnetic field. The nearest neighbour interaction now almost completely dominates which is reflected in the change in structure.

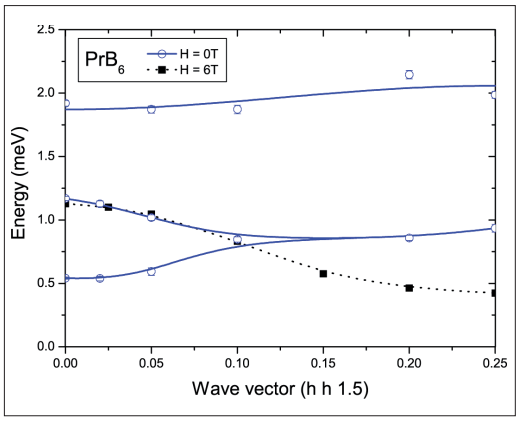

Fig.3: Dispersion of the magnetic excitations in PrB_6 at 2K. The open blue symbols show the zero field results. The filled black symbols show the results in a field of 6 tesla. The lines are guides to the eye.

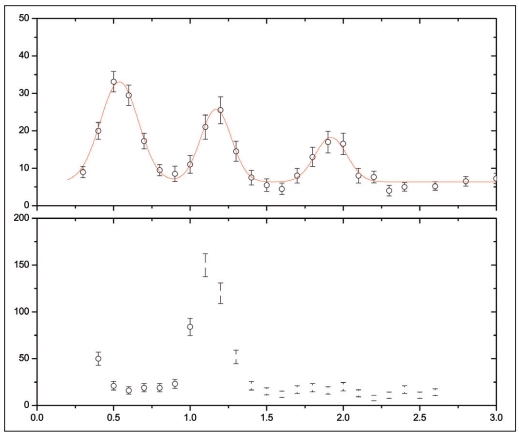

Fig.4: Typical inelastic neutron scattering spectra for PrB_6 at 2K. The data at the wave vector Q=(0 0 1.5) show that two of the three excitations in zero field are suppressed by a field of 2 tesla.

The combination of the high resolution triple-axis spectrometer and the availability of high magnetic fields at HMI have been essential in our investigations. Although the Pr ions are on a very simple structure, nevertheless the competing interactions (crystalline electric field, exchange, Zeeman and quadrupolar) lead to surprisingly complex magnetic structures. For further details, see [1]

[1] M.D. Le, K.A. McEwen, J-G. Park, S. Lee, F. Iga, K.C. Rule, submitted to *J. Phys: Condens. Matter.*, July 2007.

Corresponding author:
K. A. McEwen
k.mcewen@ucl.ac.uk

Analysis of restricted elements in plastics using XRF

C. Mans, S. Hanning, C. Simons, A. Wegner, A. Janssen, M. Kreyenschmidt
■ **Fachhochschule (University of Applied Sciences) Münster, Fachbereich Chemieingenieurwesen, Steinfurt, Germany**

Fig. 1: In a few years, even this computer will become old and contribute to the problem of electronic waste containing hazardous materials.

X-ray fluorescence analysis (XRF) has proved to be a powerful tool for a huge variety of analytical tasks in industry. One new area of application is related to the implementation of the EU directives *Restriction on use of certain hazardous substances (RoHS) [2002/96/EG]* and *Waste Electrical and Electronic Equipment (WEEE) [2002/95/EG]* which have been implemented in Germany in form of the Elektrogesetz. According to these directives, the concentrations of polybrominated biphenyls and polybrominated diphenyl ethers, lead, chromium(VI), mercury and cadmium in electronic and electrical equipment are restricted since 01.06.2006. Furthermore, all used electronic and electrical products have to be taken back and disposed by their producers. These new laws and restrictions cause technical problems as well as new challenges for the product developer as they create a need to evolve fast and economically suitable analytical tools to control a product's quality and to facilitate compliance with these regulations.

The challenge for the development of such an analytical tool is related to the large variety of materials used in this field of electronic applications. The chemical analysis of the restricted compounds might therefore be accompanied by enormous problems. Commonly used analytical methods for the determination of the regulated elements are Inductively Coupled Plasma Atomic Emission Spectroscopy (ICP-AES), Inductive Coupled Plasma Mass Spectroscopy (ICP-MS) or Atomic Absorption Spectrometry (AAS). Unfortunately these techniques require generally liquid samples. Therefore, the samples have to be digested – nowadays mostly using microwave digestion. The demand on the digestion procedure is that the material has to be brought completely into solution, which is time-consuming and costly. Furthermore the unavoidable dilution of the sample leads to a drastic rise in detection limits. For these reasons, the aim of a research project at the Laboratory for Instrumental Analysis of the University of Applied Sciences Münster was to develop an analytical method which allows the direct characterization of certain plastic materials according to EU-directives RoHS/WEEE without foregoing sample digestion.

An available analytical method which matches these demands is the X-Ray Fluorescence Analysis (XRF). Unfortunately, this method is strongly limited by the need for suitable standard materials for the calibration. In technical literature, various attempts to produce such standard materials are described. There are some standard materials available for purchase, but these are often restricted in their applicability to the RoHS/WEEE. Frequently the available materials do not contain all restricted elements and do not cover the whole concentration range necessary for the calibration. Furthermore they are available only with polyvinyl chloride (PVC) or polyethylene (PE) as matrix material, which is not sufficient for this wide range of polymer materials used in electronic industry. For these reasons, a special process was designed by the University of Applied Sciences Münster, which allows the production of plastic standards based on acrylonitrile-butadiene-styrene terpolymer (ABS), containing the regulated elements Br, Cd, Cr, Hg and Pb. ABS is a polymer commonly used as base material for e.g. housings in electrical and electronic industry. The standard materials were produced as granulates and solid bodies to potentiate the measurement of granulates as well as the measurement of bulk samples, which could be for example parts of housings etc.

Fig. 3: Produced ABS standard Materials (solid bodies) containing the regulated Elements Pb, Br, Hg, Cr, Cd

During the development of the production process it became apparent that it was impossible to add the restricted elements to the ABS without partial loss. Therefore the real concentrations of the added elements in the ABS had to be determined by alternative methods. For this special problem the Neutron Activation Analysis NAA provided by the Hahn-Meitner-Institut in Berlin was the method of choice, as especially

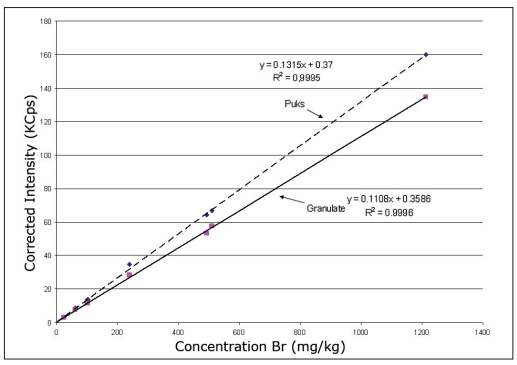

Fig. 2: Correlation of the Br-concentration in the produced standard materials determined by NAA and the measured intensities on S4 Pioneer

the determination of bromine in the ABS was not sufficient by other methods like ICP-AES or ICP-MS. NAA was chosen as this technique works without foregoing digestion of the sample and is regarded to be an absolute method.

The concentrations determined with ICP-AES (Pb) and NAA were used to calibrate the wavelength dispersive XRF S4 Pioneer (Bruker AXS) at the University of Applied Sciences Münster. The correlation of the XRF measurements with the values determined using ICP-AES and NAA showed a very good linearity as well for the produces granulates as for the solid bodies. As an example the calibration curve for Bromine is shown in Fig. 2.

The produced standard materials can be directly used to determine the concentration of the regulated elements in ABS. As determination of element concentrations in plastics is interesting for a lot of different fields in industry today, the production of further standard materials based on different plastic materials is focus of present and future research at University of Applied Sciences Münster. As these developments also need determination of the added elements by NAA, there will be a future cooperation of the Hahn-Meitner-Institut and the University of Applied Sciences Münster.

[1] C. Mans, S. Hanning, C. Simons, A. Wegner, A. Janssen, M. Kreyenschmidt, *Development of suitable plastic standards for XRF*, Spectrochimica Acta, Part B: Atomic Spectroscopy **62**B (2007) 116-122.
[2] C. Mans, S. Hanning, C. Simons, A. Janßen, M. Kreyenschmidt; *Kunststoffanalytik mit der RFA – Alles Plastik?*, Labor Praxis **10** (2006) 50-52, Journal in German

Corresponding author:
C. Mans
c.mans@fh-muenster.de

Composition profile of a wetting film in a binary liquid mixture

James Bowers[1], Ali Zarbakhsh[2], Hugo K. Christenson[3], Ian A. McLure[4], John R. P. Webster[5] and Roland Steitz[6]

■ 1 Department of Chemistry, University of Exeter, Exeter ■ 2 Department of Chemistry, Queen Mary, University of London, London ■ 3 School of Physics and Astronomy, University of Leeds, Leeds ■ 4 Department of Chemistry, University of Sheffield, Sheffield ■ 5 ISIS Facility, CLRC Rutherford Appleton Laboratory, Chilton, Didcot, UK ■ 6 HMI, SF1 and BENSC

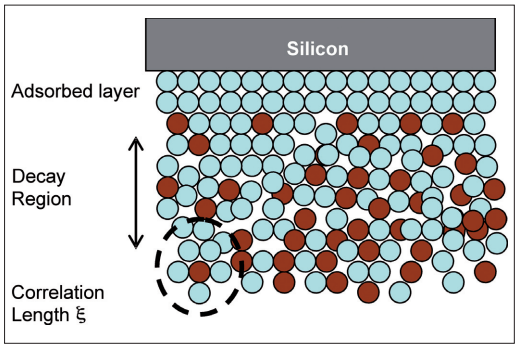

Fig. 1: Cartoon of the density in the boundary layer of a binary liquid mixture (represented by blue and brown spheres) against a solid wall (silicon substrate)

The wetting of surfaces in binary liquid mixtures has provided a rich area for fundamental studies of surface critical phenomena [1,2]. Hydrocarbon-fluorocarbon interactions are both of academic interest and practical importance with applications such as non-stick coatings, anti-graffiti paints and specialized lubricants and surfactants. Despite the absence of dipolar effects and hydrogen-bonding, alkane-perfluoroalkane systems are characterized by significant non-ideality and this gives rise to a miscibility gap with an upper critical solution temperature T_c (see Fig. 2). Close to the critical point long-range correlations in the bulk fluid dominate the adsorption behavior at a surface. Here, the density profile is expected to show universal behavior [3], decaying as an inverse power law close to the surface and showing exponential decay for distances exceeding the bulk correlation length ξ (see also Fig. 1).

Unlike the case with most liquid-vapor systems, the critical point in binary liquid systems is often at a convenient temperature and ambient pressure, thus providing ideal testing ground for theoretical predictions [1–5]. However, there are few experimental studies of wetting and adsorption in liquid-liquid mixtures away from the critical regime [2], in particular in the complete wetting regime, where adsorption is expected to be governed by long-range van der Waals forces. In our experiment at the neutron reflectometer V6 of BENSC, we studied the n-hexane and perfluoro-n-hexane system at a volume fraction of n-hexane $\phi_H = 0.25$ (in the complete wetting regime, far from the critical $\phi_H = 0.50$). See also crosses in Figure 2.

The reflectivity data obtained allowed for the determination of the composition profile of the wetting film [7]. Near the coexistence limit T_0, the composition of the liquid boundary layer was found to be different from the bulk fluid for distances up to $z \approx 100\text{-}120$ nm. The neutron reflectivity curves recorded from the system are displayed in Fig. 3. They show significant changes close to the critical edge (inset). The volume fraction profiles derived from the multilayer fits in Fig. 3 are shown in Fig. 4a. Far from coexistence, i.e. $T/T_c > 1$, there is a thin adsorbed film with the hexane content decaying exponentially towards the bulk. As T approaches T_c the decay length of the exponential increases as does the hexane content. For $T < T_c$ the decay length remains constant but the thickness and n-hexane content of the film increase with decreasing T. Furthermore, the advancement of the critical edge indicates the presence of a long-range effect on the density profile. There must be an extensive region with n-hexane content greater than that of the bulk, but

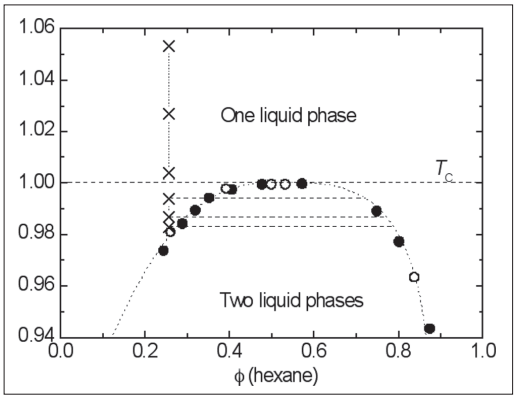

Fig. 2: Phase diagram displayed as T/T_c against the hexane volume fraction for the mixtures n-hexane-h_{14} (•) or n-hexane-d_{14} (o) + perfluoro-n-hexane. The dotted curve is the common curve for this and related mixtures [6]. The (x) are experimental points and the horizontal lines determine the composition of the hexane-rich phase at coexistence.

different from that of the wetting film that emerges at the coexistence limit. Only in the inner region, next to the substrate surface, does the composition of the film approach that of the n-hexane-rich phase, which phase separates at T_0 (or $T/T_c = 0.98$ for $\phi_H = 0.25$, see Fig. 2). The horizontal regions of the profiles for small z result from minimising the number of parameters in the fitting procedure.

The reflectivity curves were fitted using three modeling strategies, resulting in profiles displaying very much the same characteristic features (Figure 4). The profiles in Fig. 4b and 4c give the same high-quality fits to the reflectivity data as the fit shown on Fig. 3, which corresponds to the profile in Fig. 4a. All profiles show the growth

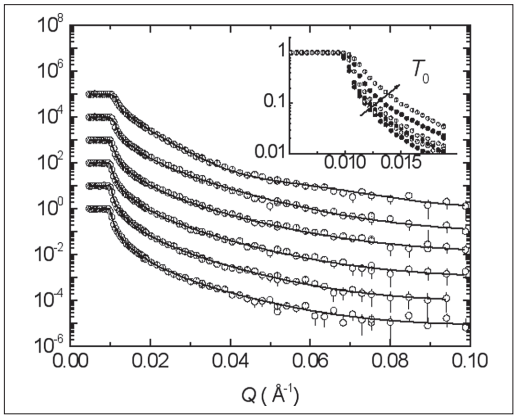

Fig. 3: Reflectivity measured along the path indicated by crosses in Fig. 2; from bottom to top, $t_0 = |T\text{-}T_0|/T_0 = 7.38 \times 10^{-2}$, 4.70×10^{-2}, 2.32×10^{-2}, 1.32×10^{-2}, 5.81×10^{-3}, and 1.91×10^{-3}. The solid lines are fits corresponding to the volume fraction composition profiles of Fig. 4a. The inset shows how the critical edge advances as the coexistence limit $T_0 = 0.98\ T/T_c$ for ϕ (hexane) = 0.25 is approached. For that composition, $T_c = 14.39 \pm 0.05$ °C, and T_0 is 8.93 ± 0.05 °C.

of a wetting layer close to the interface followed by a long decay to the bulk composition. These features occur on length scales greater than the nominal minimum resolution ($2\pi/Q_{max}$) of 60 Å.

The surface excess, i.e. the enrichment of hexane at the interface, was computed from the profiles shown in Fig. 4 as $\Gamma = \int_{z=0}^{\infty}(\phi - \phi_B)c_H dz$, where ϕ_B is the bulk volume fraction and c_H is the concentration of pure hexane. Γ obeys the predicted power law $\Gamma = \Gamma_0 t_0^m$ as a function of distance from coexistence with $t_0 = |T\text{-}T_0|/T_0$.

At small t_0 for $T < T_c$, the exponent m is close to –1/3, a value consistent with van der Waals complete wetting. For larger t_0, $m >> -1/3$, indicating a

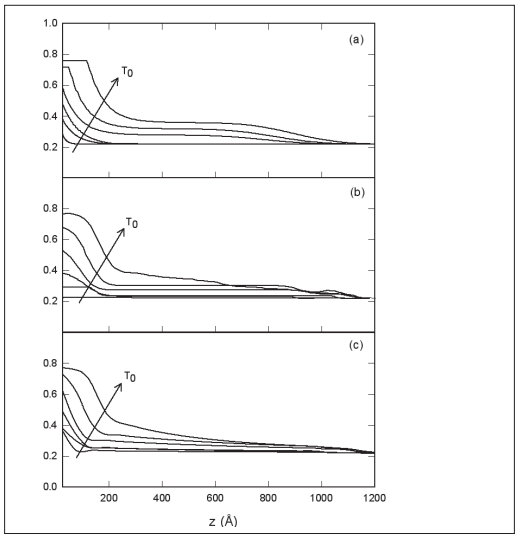

Fig. 4: Volume fraction composition profiles corresponding to the multilayer fit in Fig. 3 (a), from the unbiased fit (b), and from the analytical fit (c). The arrows show the evolution as the coexistence point is approached.

crossover in wetting behavior. We note, however, that these conclusions should be considered with caution as the Lifshitz theory of van der Waals forces cannot be strictly applied to a system in which the density profile decays so gradually into the bulk. In such a case it is not possible to define a sharp interface between the bulk solution and the adsorbed region. Moreover, it is not clear up to what extent the wall and the bulk fluid at large z compete in determining the strength of the z^{-3} potential.

[1] Bonn, D.; Ross, D. Rep. Prog. Phys. **64**, (2001).
[2] Law, B. D. Prog. Surf. Sci. **66**, (2001).
[3] Fisher, M. E.; De Gennes, P. G. C. R. Acad. Sci. (Paris) Ser. B **287**, 207,(1978); Rowlinson, J. S.; Widom, B. Molecular Theory of Capillarity; Dover: Mineola, NY, 2002.
[4] Zhao, H; Penninckx-Sans, A.; Lee, L.-T.; Beysens, D.; Jannink, G. Phys. Rev. Lett. **75**, (1995).
[5] Fenistein, D.; Bonn, D.; Rafaï, S.; Wegdam, G. H.; Meunier, J.; Parry, A. O.; Telo da Gama, M.; Phys. Rev. Lett. **89**, 096101, (2002)
[6] Bowers, J.; Zarbakhsh, A.; Christenson, H. K.; McLure, I. A.; Webster, J. R. P.; Steitz, R. Phys. Rev. E **72**, 041606 (2005).
[7] Bowers, J.; Zarbakhsh, A.; McLure, I. A.; Webster, J. R. P.; Steitz, R.; Christenson, H. K. J. Phys. Chem. C **111**, 5568 (2007).

Corresponding author:
R. Steitz
steitz@hmi.de

Higher and Higher: Momentum-Resolved High-Resolution Spectroscopy of Elementary Excitations using the Neutron Resonance Spin-Echo Method

K. Habicht[1], T. Keller[2, 3], S.P. Bayrakci[2], P. Aynajian[2], L. Boeri[2], S.K. Bose[2], B. Keimer[2] und F. Mezei[1]

■ 1 HMI, SF1 ■ 2 Max-Planck-Institut für Festkörperforschung, Stuttgart ■ 3 ZWE FRM II, TU München

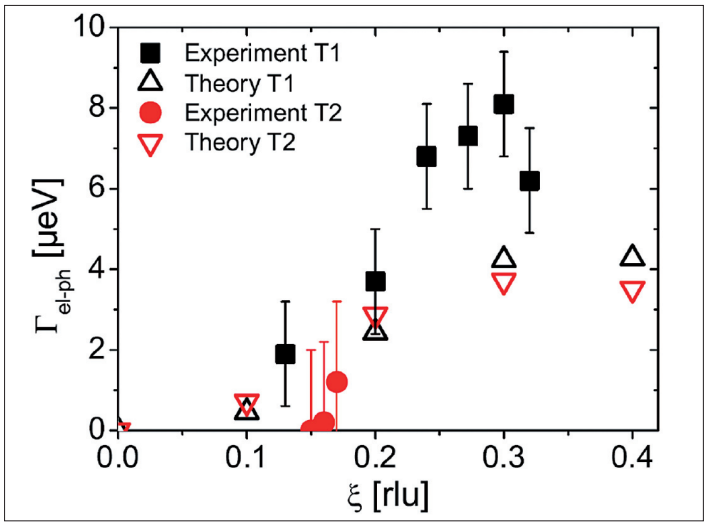

Fig. 1: Contribution of the electron-phonon interaction to the linewidth of transverse acoustic [ξξ0] phonons in Pb with different polarization vectors T1 and T2: experimental data compared to ab-initio theoretical predictions.

From a microscopic point of view, transport phenomena in solid state physics, such as thermal or electrical conductivity, are governed by the interaction between quasiparticles or their interaction with other real particles. Heat in a material can be transported by the propagation of quantized lattice vibrations, i.e. phonons. This phonon propagation, and thus the lifetime of the quasiparticles, is limited by the interaction with other thermally excited phonons as is the case in anharmonic crystals. Electrical conductivity is limited by scattering processes of electrons with phonons playing a crucial role in superconductivity of elemental metals. Likewise in a magnetic material collective spin excitations (magnons) may interact with each other. All these diverse types of interactions (phonon-phonon, electron-phonon, and magnon-magnon) can be studied by measuring the quasiparticle lifetime which is inversely proportional to their linewidth in energy. While the energy of the elementary excitations as a function of wavevector (dispersion relation) is easily accessible with well established neutron scattering techniques such as triple-axis spectroscopy (TAS), higher energy resolution is mandatory for the study of their energy widths or lifetimes.

Increasing the resolution is usually at the cost of intensity of the probing neutron beam. The Neutron Spin Echo method allows overcoming this restriction in that it decouples the energy resolution from the intensity by using polarized neutrons. High energy resolution is here achieved by measuring the spread in Larmor precession angles of neutrons travelling in well defined magnetic field regions before and after the sample. The Neutron Resonance Spin-Echo technique (NRSE) is a sophisticated technical variant ideally suited to investigate dispersive excitations since *spin-echo focussing* onto the phonon branches is easily realized by tilting of compact resonance frequency spin-flippers. Combining NRSE and TAS instrumentation offers the highest resolution available for lifetime studies of dispersive excitations.

The first realization of the NRSE-TAS technique has been implemented at the cold neutron triple axis instrument V2/FLEX at HMI. Initial experiments focused on the temperature dependence of phonons along the main crystallographic directions in single crystal Pb [1]. Broadening of the one-phonon peaks due to lattice anharmonicity (phonon-phonon interaction) resulting in Lorentzian linewidths could be measured with high accuracy. A thorough understanding of resolution effects in NRSE-TAS type experiments is a necessary prerequisite to separate intrinsic lifetimes from resolution effects. This is provided by a general analytical approach developed at HMI, which identified systematic instrumental effects, sample mosaicity and curvature of the

dispersion surface to enter into the resolution function and allows one to correct experimental raw data. Since NSE is sensitive to the intermediate scattering function directly such correction requires no deconvolution as has been proven for the case of dispersive excitations [2].

The difference in linewidths for a phonon mode above and below the superconducting transition temperature T_C is a direct measure of the electron-phonon contribution to the linewidth. Due to Cooper-pair formation the phonon decay channel via e-p interaction is forbidden below T_C. The experiments performed at V2/FLEX could already establish a 6 μeV upper limit for the change in linewidth due to electron-phonon interaction for a particular mode, the transverse acoustic [0.1 0.1 0] phonon. In collaboration with the MPI Stuttgart pioneering experiments could be performed with the new NRSE based instrument TRISP at FRM II. This instrument benefits from a substantial increase in neutron flux and offers access to thermal neutron wavelengths. The electron-phonon interaction in the BCS superconductor Pb could be studied in a wide momentum range [3]. For the first time a detailed comparison between theoretical *ab-initio* model calculations and momentum-resolved experimental data became possible (Fig. 1). This comparison shows that the q-dependence of the electron-phonon contribution to the linewidth is in general satisfactorily described by theory. Quantitatively however, the theory yields smaller values than experimentally observed.

The NRSE method is also very well suited to investigate spin waves in antiferromagnets. Recently it has been applied in measurements of the prototype antiferromagnet MnF_2 [4]. Due to access to thermal neutron wavelengths earlier experiments performed at V2/FLEX (restricted to a wavevector range less than 0.2 reciprocal lattice units) could be extended to investigate magnon lifetimes over the whole Brillouin zone. Both wavevector and temperature dependence were extensively investigated. As a surprising result, the experimental data (Fig. 2) is best described by a theoretical model which is based on scattering processes of magnons with longitudinal spin fluctuations and not by magnon-magnon interaction.

These experiments demonstrate that the spin echo method allows a completely new experimental access to the understanding of important microscopic phenomena such as superconductivity or dynamics in magnetism and mark the beginning of a new chapter in neutron scattering research.

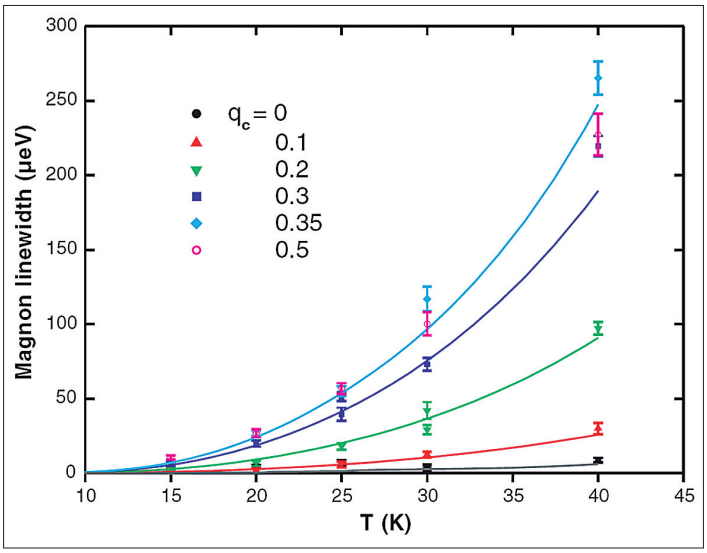

Fig. 2: Temperature dependence of magnon linewidths in MnF_2 for various wavevectors q_c along the crystallographic c-direction. The curves represent theoretical model calculations.

[1] K. Habicht, R. Golub, F. Mezei, B. Keimer, and T. Keller, Phys. Rev. B **69**, 104301 (2004).
[2] K. Habicht, T. Keller, and R. Golub, J. Appl. Crystallogr. **36**, 1307 (2003).
[3] T. Keller, P. Aynajian, K. Habicht, L. Boeri, S.K. Bose, B. Keimer, PRL **96**, 225501 (2006)
[4] S.P. Bayrakci, T. Keller, K. Habicht, B. Keimer, Science **312**, 1926 (2006)

Corresponding author:
K. Habicht
habicht@hmi.de

Sodium ordering and the control of properties in sodium cobaltate

D. J. P. Morris[1], M. Roger[2], D. A. Tennant[1,4], M. J. Gutmann[5], J. P. Goff[3], J.-U. Hoffmann[1], R. Feyerherm[1], E. Dudzik[1], D. Prabhakaran[6], A. T. Boothroyd[6], N. Shannon[7], B. Lake[4,8] & P. P. Deen[9]

■ 1 HMI, SF2 ■ 2 CEA Saclay, France ■ 3 Royal Holloway, University of London, UK ■ 4 Institut für Festkörperphysik, Technische Universität Berlin, Germany ■ 5 ISIS, Didcot, UK ■ 6 Clarendon Laboratory, Oxford, UK ■ 7 University of Bristol, UK ■ 8 HMI, SFN1 ■ 9 ILL, Grenoble, France

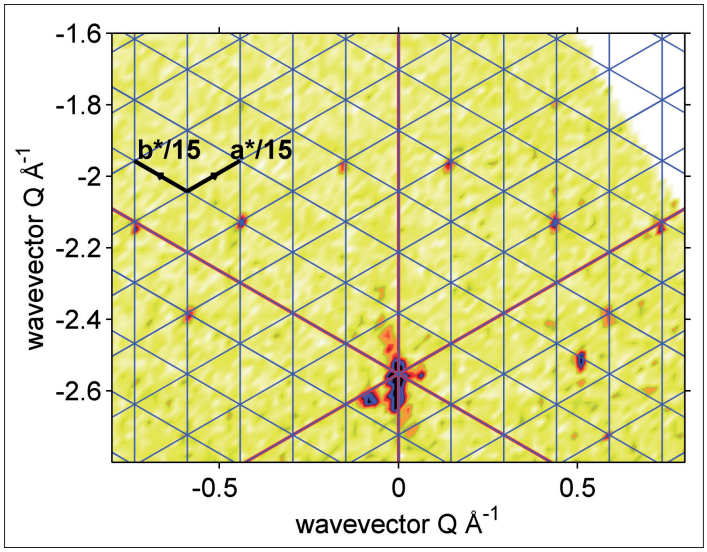

Fig. 1: Superstructure peaks observed for $Na_{0.75}CoO_2$ on E2 at HMI at 1.5K in the (hk0) plane. The high **Q**-resolution allowed the commensurability of this structure to be observed by placing a commensurate grid (**a***/15 × **b***/15) over the data.

Sodium cobaltate, Na_xCoO_2, has attracted much interest in the past decade due to the possibilities of thermoelectric applications [1] and interplay between magnetism and superconductivity leading to comparisons with the superconducting cuprates [2].

The structure is made up of triangular layers of CoO_2 separated by a sodium layer of variable concentration. Due to this structure it was expected to show two-dimensional magnetism. Whereas magnetic inelastic neutron scattering measurements showed that the in-plane magnetic coupling is comparable to that out-of-plane [3], implying different underlying physics to that seen in the cuprates.

In 2003 superconductivity was discovered in the hydrated material, $Na_{0.35}CoO_2{\cdot}1.3H_2O$ [2]. Early understanding was that the water molecules created a spacer layer screening the cobalt from the pair breaking potential due to the Na^+ ordering. This was backed up by the discovery that the monohydrate system (H_2O intercalated into the Na layer rather than between Na and CoO_2 layers) fails to superconduct. Recent work, however, has shown that the water also plays a chemical role in the superconducting samples with the intercalation of oxonium ions, H_3O^+, into the Na layer.

Recent studies have shown one way of obtaining the properties of a good thermoelectric material is via phonon-glass-electron-crystals (PGEC). Such materials form electrically conductive cages around a free atom which can 'rattle' scattering thermal phonons. One explanation for Na_xCoO_2 being a good thermoelectric is that it is a PGEC but lacks the usual 'rattler' cages [4]. Other possible explanations for the thermopower have also developed and gained popularity for example involving spin entropy.

The role of sodium ordering on the physical properties and the principles behind the ordering was also not well understood, although was widely recognised as playing an important role in the broader physics. This had previously been studied using electron diffraction, powder neutron diffraction and single crystal hard x-ray diffraction but the ordering principles had not been deduced. Our approach was to take high quality single crystals and observe the spatial sodium ordering using complementary diffraction techniques; neutron Laue diffraction on the SXD instrument at ISIS and E2 at HMI and hard x-ray diffraction on MAGS at BESSY [5].

With SXD, a large three-dimensional volume of reciprocal space is measured giving more information about the superstructure than the previous techniques used since a large number diffracted peaks (main Bragg peaks and superstructure peaks) are obtained. In a sample of concentration x=0.92 a 12-spot ring surrounding the main Bragg peak positions at base temperature and superstructure peaks at 0.2 r.l.u. (reciprocal lat-

tice units) at room temperature were measured. The 12-spot ring was also measured in a sample of concentration $x=0.75$ at base temperature and also at 150 K. Then using E2 it was possible to zoom into a plane of reciprocal space giving higher resolution in wave-vector transfer (**Q**). With this information we were able to determine that this ordering is commensurate (see Fig.1). Also following the peak heights with varying temperature told us that we were dealing with a first order transition at approximately 285 K. Using single crystal hard x-ray measurements on MAGS allowed precise temperature dependence measurements to be made. This showed a substantial hysteresis in the superstructure peak intensities across the transition.

By application of electrostatics, involving short-range and long-range potentials on the sodium cobaltate structure, the ordering principles were studied. The sodium ions have two possible sites; Na^1 on top and below a neighbouring cobalt ion, and Na^2 which is a lower energy site away from nearest neighbour cobalt ions. It was found that vacancies in the sodium layer become attractive at very short distances since the promotion of a sodium ion onto Na^1 sites become energetically favourable. The long-range Coulomb interactions then allow these clusters to condense out onto a long range order. One ground state structure that condenses out of this model is a square trivacancy structure with concentration $x=0.80$. By further calculating the potential gradient on the cobalt ions due to the Na ordering it was possible to see that the CoO_2 layer is buckled by the underlying sodium cluster (see Fig.2). Our low temperature data proved extremely sensitive to this buckling, with the Fourier transform of the trivacancy structure requiring the cobalt ions to be buckled by less than $0.01c$ in order to give good agreement with diffraction data (c being the c lattice parameter, ~10.82Å) [5].

Calculating the Coulomb landscape on the cobalt layer it is then possible to see how the partial cobalt valences, reported in NMR measurements, are realised. Also the resulting potential wells are large compared to hopping frequencies, therefore spins can become localised. This occurs with the same periodicity as the sodium ordering and can readily explain the dimensionality of the magnetism since in plane well separation is approximately equal to the c-lattice parameter. The buckling of the CoO_2 layer forms cages around the Na_1 ions (red spheres in fig. 2) giving rise to the rattler sites missing from previous reports of PGEC thermoelectric behaviour in this material as well as conduction pathways within the Coulomb landscape.

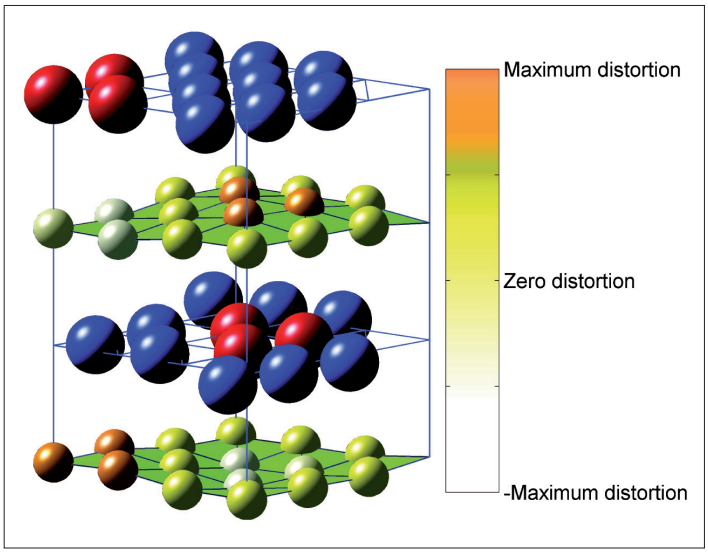

Fig. 2: Unit cell for $x=0.80$ trivacancy superstructure used to model the low temperature phase for $Na_{0.75}CoO_2$ and $Na_{0.92}CoO_2$. The colour scale shows the buckling of the CoO_2 layer (oxygens are ommited for clarity) that form cages allowing Na to rattle.

To summerise, the sodium ordering has been understood with complementary techniques of neutron and x-ray diffraction with application of electrostatics. This then sheds new light on the magnetism, thermopower, and importance of ionic ordering in this type of system.

[1] I. Terasaki, et al. Phys. Rev. B. **56**, R12685–R12687 (1997)
[2] K. Takada, et al. Nature. **422**, 53–55 (2003)
[3] S. P. Bayrakci, et al. Phys. Rev. Lett. **94**, 157205 (2005)
[4] K. Takahata et al. Phys. Rev. B. **61**, 12551–12555 (2000)
[5] M. Roger, et al. Nature. **445**, 631-634 (2007)

Corresponding author:
D. J. P. Morris
jonathan.morris@hmi.de

Spin-state polaron as a precursor to ferromagnetism and metallicity in hole-doped $LaCoO_3$

A.Podlesnyak[1], M.Russina[2], K.Conder[3], E.Pomjakushina[3], P.Allenspach[3] and D.I.Khomskii[4]

■ 1 HMI SF2 ■ 2 HMI SF1 ■ 3 Laboratory for Developments and Methods, Paul Scherrer Institut, Villigen PSI, Switzerland. ■ 4 II Physikalisches Institut, Universität zu Köln, Köln, Germany.

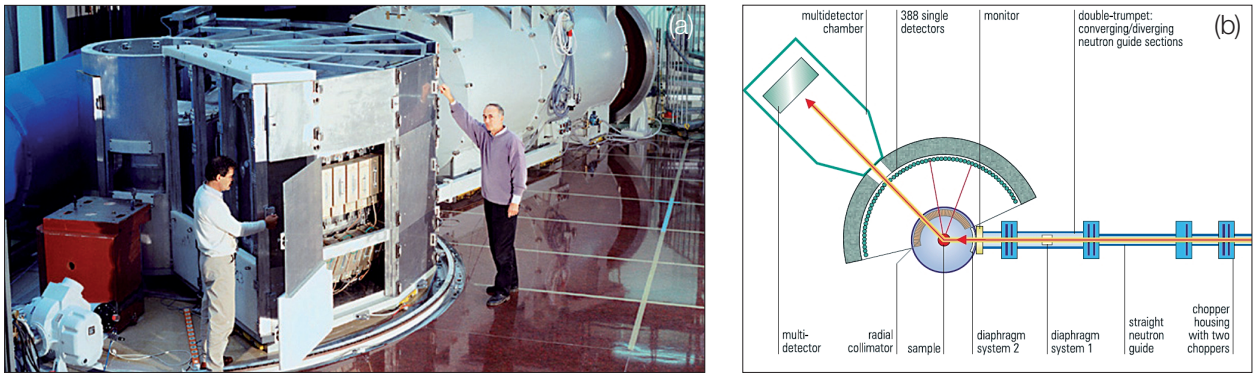

Fig. 1: a) The high-resolution time-of-flight spectrometer V3/NEAT b) Schematics of a direct time-of-flight spectrometer. The choppers define the energy and the pulse width of the incident neutrons. The monochromatic neutron pulses are then scattered from the sample and are detected by arrays of neutron counters covering a large solid angle. The energy transfer $\hbar\omega$ and the modulus of the scattering vector **Q** are then determined by the flight time of the neutrons from the sample to the detector and by the scattering angle Θ at which the detector is positioned, respectively.

Nanostructured magnetic materials form a novel type of systems where fundamental properties can be tuned to desired requirements on the molecular level. It makes these materials of particular interest for applications in such fields as molecular electronics or quantum computing. Doped perovskites $La_{1-x}Sr_xCoO_3$, compounds where magnetic nanoclusters of 20-30Å coexist in a nonmagnetic matrix [1], can serve as a naturally occurring analogue to artificially fabricated heterostructures. Already a slight variation of the doping degree strongly influences the interactions in- and between the clusters leading to dramatical changes of the macroscopic properties, such as value and temperature dependence of magnetization.

Most of the investigations up to now have been focused on the relatively high composition range above x=0.1, where it is believed that embedded spins already form short-range-ordered ferromagnetic clusters. However, one intriguing point was discovered in 1996 and apparently forgotten later. Namely, already lightly doped materials, with an estimated concentration of x~0.002 (i.e. two holes per thousand Co^{3+} ions) exhibit paramagnetic properties at low temperatures, in strong contrast to the diamagnetic $LaCoO_3$ [2]. The few embedded spins in a nonmagnetic background would give order of magnitude smaller magnetic susceptibility than it was observed. With this controversy in mind, we undertook an inelastic neutron scattering (INS) study with the goal to identify the energy spectrum and magnetic state of the excited state of cobalt ions in lightly doped $La_{0.998}Sr_{0.002}CoO_3$. The measurements with and without application of magnetic field have been performed on the cold neutron time-of-flight spectrometer NEAT at HMI (Fig. 1). In the view of the low signal the successful optimization of NEAT for these types of studies including the development of the new data collection approach was of crucial importance. The details of the experiments are described in original publications [3-5]. In this report we briefly discuss the obtained result.

Undoped $LaCoO_3$ with perovskite structure contains Co^{3+} ions with six electrons in $3d$ orbitals, octahedrally surrounded by six O^{2-} ions. Two of the $3d$ orbitals ($3d_{x^2-y^2}$ and $3d_{z^2}$, which are called e_g) point directly toward the O^{2-} ions. The other three orbitals ($3d_{xy}$, $3d_{xz}$, and $3d_{yz}$, which are called t_{2g}) lie between the O^{2-} ions. In the crystal field of the six O^{2-} ions the degeneracy of the five $3d$ orbitals is lifted. The latter three of these orbitals are now lower in energy than the former two. The intra-atomic ex-

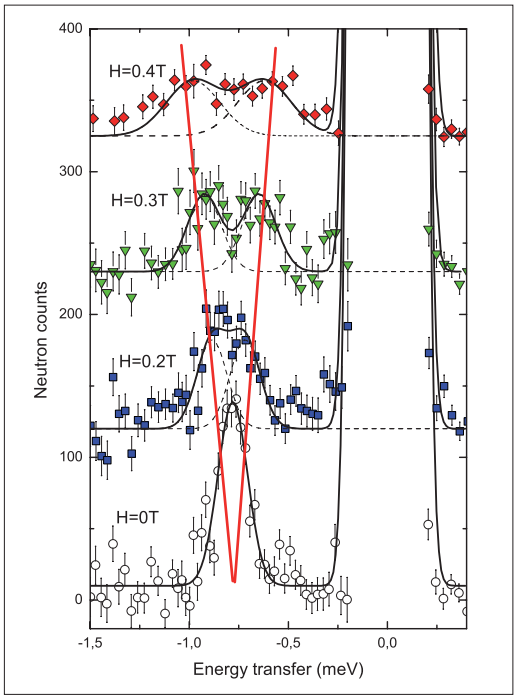

Fig. 2: Evolution of the INS in the external magnetic field at T=2 K.

change interaction and the octahedral crystal-field interaction determine the three possible choices of the orbital occupations by electrons. One of these configurations of Co^{3+} (with 6 d-electrons) has the maximum spin S=2 and is called high-spin (HS). The others configurations are called low-spin (LS) and intermediate-spin (IS) because they contain zero and two unpaired electrons, respectively. When holes are put into these orbitals by replacing the trivalent La^{3+} ions with divalent Sr^{2+} ions, the compound becomes a mixed valence system with both Co^{3+} and Co^{4+}. The description of the magnetic states requires an assignment of the spin state to both Co^{3+} and Co^{4+} ions. The number of possible configurations of the system gives rise to discrete energy levels E_i which can be determined by inelastic neutron scattering. The idea of INS experiment is rather simple. The excited level at energy ΔE results in an inelastic peak in the spectrum of scattered neutrons at an energy transfer $\pm\Delta E$. The position of the peak is determined by the energy gap between two configurations.

In contrast to the parent compound $LaCoO_3$, where no excitations have been found for temperatures T<30K [4], in the doped system with the Sr concentration of only 0.2% an inelastic peak at the energy transfer ΔE~0.75 meV was observed already at T=1.5K. Surprisingly, the intensity of the ΔE excitation is much higher than it was expected from an estimated concentration of doped holes per Co site. With the application of a magnetic field

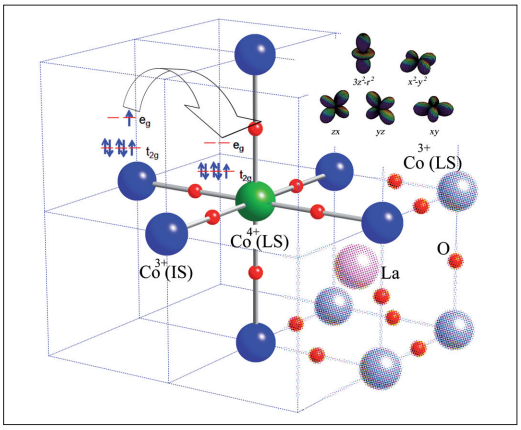

Fig. 3: Schematic view of a possible state of spin-state polaron. The scheme showing the process of electron (hole) hopping on the background of the Co^{3+}(IS) and Co^{4+}(LS) ions. Five 3d orbitals are shown in the right upper corner.

we observed strong Zeeman splitting of the inelastic peak indicating an *unusually high magnetic moment* $gS\sim15\mu_B$ (see Fig. 2). The value of the magnetic moment cannot be described by single Co^{4+} ion in any spin state. In contrast, contribution of several Co-ions, i.e. the formation of the magnetic clusters is required to explain the experimental data. Neighboring LS-Co^{4+} ion and IS-Co^{3+} ion can share an e_g electron by swapping configuration, as shown in Fig. 3. The t_{2g} electrons, in their turn, couple ferromagnetically via double exchange interaction. Therefore, we propose that the *holes introduced in the LS state of* $LaCoO_3$ *are extended over the neighboring* Co *sites forming spin-state polarons and transforming all the involved* Co^{3+} *ions to the IS or HS state (Fig. 3)*. Spin-state polarons behave like a few nanometer size magnetic nanoparticles embedded in an insulating nonmagnetic matrix. The addition of charge carriers leads to grows of such spin-state polarons and finally results in a metallic state with long-range FM order for $x>0.18$ [1]. Our results show remarkable importance of intrinsic inhomogeneities for the governance of macroscopic properties and functionality of doped cobaltites. The tuning of the characteristics of spin-based inhomogeneities in the desired way opens bright perspectives for novel technological applications of these materials.

[1] J. Wu, et al., Phys. Rev. Lett. **94**, 037201 (2005).
[2] S. Yamaguchi, et al., Phys. Rev. B **53**, R2926 (1996).
[3] A. Podlesnyak, et al., JMMM **310**, 1552 (2007).
[4] A. Podlesnyak, et al., Phys. Rev. Lett. **97**, 247208 (2006).
[5] A. Podlesnyak, et al., to be published.

Corresponding author:
A. Podlesnyak
andrei.podlesnyak@hmi.de

Correlation between Icosahedral Short Range Order, Glass Forming Ability and Crystallization of Zr-Ti-Mi-Cu-(Be) Glasses

N.Wanderka, S. Mechler
■ HMI, SF3

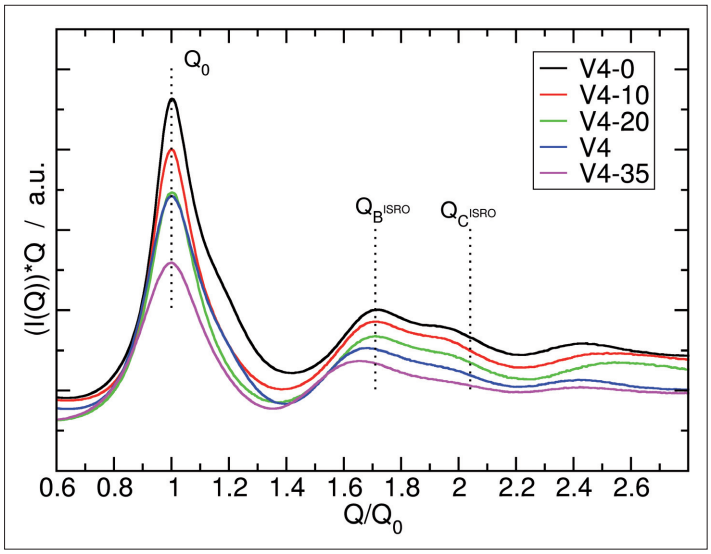

Fig. 1: Interference function $I(Q)*Q$ of various Zr-Ti-Ni-Cu glasses with different Be content (in at.%) amorphous glasses. Be free glass is also shown. The values Q_B and Q_C ^{ISRO} mark the positions of diffuse maxima which according to [3] are indicative for icosahedral short range order of the amorphous phase.

Zr-based metallic glasses can be produced by cooling liquid melts with cooling rates comparable to those of oxide glasses. They are of great technical and physical interest because of their extraordinary properties like high strength, elasticity and low viscosity. However, for their potential application, knowledge about the correlation between structure and thermal stability against crystallisation is necessary. An important parameter for such alloys is the structural icosahedral short-range order (ISRO). ISRO of the glassy phase hinders the formation of intermetallic crystalline phases but leads to formation of quasicrystals. The stable $Zr_{41.5}$–$Ti_{41.5}$-Ni_{17} quasicrystal has ideal ISRO [1]. If the composition of this alloy is altered, e.g. by addition of misfit atoms like Be, the deterioration of the ISRO structure hinders the formation of quasicrystals and therefore the glassy phase is preferred.

To get more insight into the role of ISRO on the thermal stability of glasses we investigated the effect of Be addition to Zr-Ti-Ni-Cu model alloys by X-ray diffraction (XRD) combined with transmission electron microscopy (TEM). The structure of such glasses with different Be content is indicated by the interference functions $I(Q)$ in Fig.1, which were derived from corresponding TEM-selected area electron diffraction images. The existence of the third maximum Q_C^{ISRO} is indicative for ISRO. Be free glass has a significant third maximum Q_C^{ISRO} which indicates high degree of ISRO. Be containing glasses show a decrease of the intensity of the third maximum. With an increase of Be content, the degree of ISRO decreases and for the alloy with Be contents > 25 at%, the third maximum is practically vanished.

We found that the Be free glass easily transforms polymorphously into a quasicrystalline phase during thermal treatment because their ISRO facilitates the nucleation of quasicrystals. The TEM micrograph in Fig. 2 shows the microstructure of the completely crystallised Be free glass The diffraction pattern (inset in Fig. 2) taken from one of the grains shows the tenfold symmetry of an icosahedral quasicrystalline phase. In contrast Be rich glasses are very stable against crystallization and crystallise preferably into intemetallic phases, because the misfit of Be atoms deteriorates the ISRO of the glass and thus impedes the formation of quasicrystals.

Our results fit to the model of geometric frustration, which describes metallic glasses as “highly defective” quasicrystals [2], i.e. as quasicrystals for which the ISRO structure is degraded by misfit atoms. This model can be used as a rule for the design of metallic glasses based on the stable $Zr_{41.5}$–$Ti_{41.5}$-Ni_{17} quasicrystal. Fig. 3 shows a flowchart starting from the composition of this quasicrystal which is altered by the addition of Be, Cu and Al or by change of the element ratios of the composition. Alloys indicated by red colour in Fig. 3 form preferably quasicrystals while alloys indi-

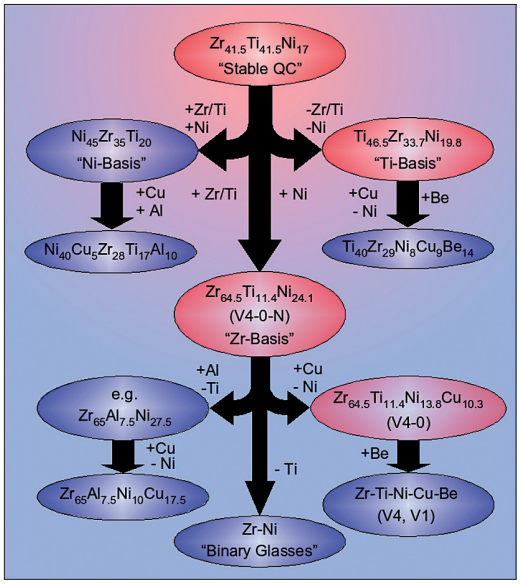

Fig. 3: Flow-chart for the structural alteration of quasicrystals towards metallic glasses as a hint for the design of metallic glasses. Starting from the composition of the stable $Zr_{41.5}$–$Ti_{41.5}$-Ni_{17} quasicrystal the structure is altered by the addition of Be, Cu and Al or by change of the element ratios of the composition, that disturb the ISRO. Alloys indicated by red colour form preferably quasicrystals while alloys indicated by blue colour are good glass formers.

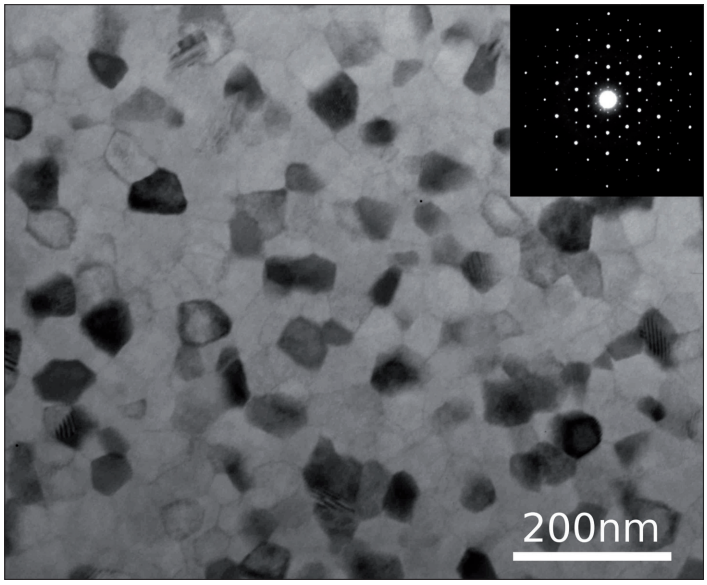

Fig. 2: Bright field TEM image of the microstructure of the Be free Zr-Ti-Ni-Cu-glass after heat treatment with the corresponding SAED image of one icosahedral quasicrystal in the inset.

cated by blue colour are good glass formers. The flow scheme reveals, that the more the structure of the ideal, stable quasicrystal is disturbed, the less stable they are until the glass becomes the preferable structure of the alloy.

More detailed investigations of metallic bulk glasses including the stability against thermal treatments can be found in the thesis of S. Mechler, TU Berlin, January 2007 [4].

[1] K.Kelton, Intermetallics **14** (2006) 996
[2] M.V. Jaric, Introduction to quasicrystals, Vol. 1 (Academic Press Inc., San Diego, 1988)
[3] S.Sachdev and D. Nelson, Phys. Rev. B **32** (1985) 1480
[4] S. Mechler, Ph.-D. Thesis, TU Berlin, January 2007

Corresponding author:
N. Wanderka
wanderka@hmi.de

Energy-selective neutron radiography

N. Kardjilov[1], A.Hilger[1], I. Manke[1,2], M. Strobl[3], W. Treimer[3], J. Banhart[1,2]
■ 1 HMI, SF3 ■ 2 Technische Universität Berlin ■ 2 University of Applied Sciences (TFH) Berlin

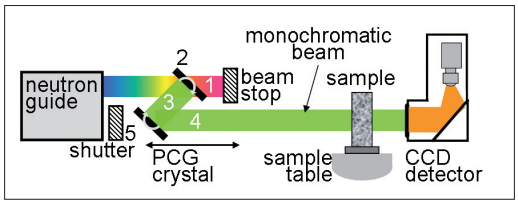

Fig. 1: Schematic sketch of CONRAD including the double monochromator device: (1) upper guide and neutron beam (2) first PG(002) monochromator, (3) diffracted monochromatic neutron beam, (4) second PG(002) monochromator, (5) lower guide and shutter of lower part of the neutron beam

Neutron imaging and especially neutron tomography gained a lot of importance in neutron instrumentation for scientific and industrial applications within the last decade. Monochromatic neutrons, however, have not been in the focus of mainstream developments due to the high intensity losses and correspondingly longer measuring times. In spite of that the neutron radiography and tomography with a monochromatic beam shows promising results in comparison to the standard technique where a white beam is used.

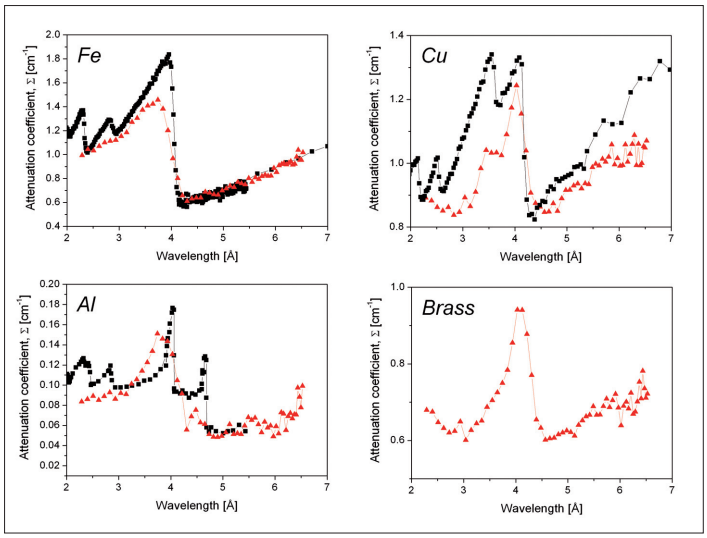

Fig. 2(a) – (d): Tabulated (dark) and radiographically (light) measured attenuation coefficients of Al, Fe, Brass and Copper. The measured values are smeared due to the rather large mosaic spread of the C- crystals.

In the case of polychromatic neutron tomography severe problems for quantification of components of a sample in neutron imaging arise from scattering effects and beam hardening – an effect caused by the fact that the attenuation coefficients are different for different energies present in the beam. The use of monochromatic radiation avoids beam hardening, and the use of wavelengths beyond the Bragg edges of a material avoids Bragg scattering if $\lambda > 2d_{max}$, where d_{max} is the biggest crystal lattice spacing of the sample material (see Table 1). For crystalline solids, these effects and strong incoherent scattering from hydrogenous materials give rise to unwanted background scattering. Monochromatic cold neutrons allow for a much better quantification and are much more sensitive to inhomogeneities in samples. Therefore, a double monochromator option was designed and set up at the neutron radiography instrument CONRAD at HMI [1].

The first measurement position of CONRAD immediately behind the neutron guide was used to install a double monochromator device as shown in Fig.1. Both crystals of the device can be rotated to chosen Bragg angles; the second one can additionally be positioned along the original beam direction in order to reflect the monochromatic beam coming from the first crystal into the initial beam path of the CONRAD instrument. This construction enables one to choose a monochromatic beam with a defined wavelength band ($0.1 < \Delta\lambda/\lambda < 0.01$) between 2.0 Å and 6.5 Å. This wavelength range (depending on the Bragg angle) includes the Bragg edges of many important engineering materials like e.g. Al, Brass (CuZn), Cu and Fe.

Material (hkl)	Al (111)	C (001)	Cu (111)	Fe (110)	β-CuZn (110)
Cut-off, d_{max} [Å]	4.68	6.71	4.17	4.08	4.20

Table 1: Bragg cut-offs of important engineering materials

Quantitative measurements were performed on test samples of Al, Fe, Brass and Copper and the data compared with tabulated values. Figs.2a–2d show the results (for brass tabulated values could not be found). The worse resolution

is due to the broad mosaic spread of the graphite crystals, however, a smaller mosaic spread would decrease the reflected intensity and increase the exposure time for radiography and tomography.

The advantage of such a continuously adjustable wavelength is apparent. Different parts of an object under investigation having very similar attenuation coefficients can be made transparent at a certain wavelength (cp. the attenuation of copper at $\lambda = 3.4$ Å and $\lambda = 4.2$ Å, and for steel at $\lambda = 4.2$ Å and $\lambda = 4.6$ Å) or enhanced using another wavelength, where the particular attenuation differs much more, see Fig. 3. Moreover, the method gives the possibility to distinguish between alloys like Cu and ZnCu (Brass). Additionally, the attenuation of PE is nearly constant within narrow wavelength band. So it is possible to eliminate scattering from H-containing parts in a radiography (and tomography) using proper wavelength for other materials that show high contrast in the pictures, see Fig. 3 (right).

Material stress and strain regions in samples usually require point-like scans of neutron diffraction to determine the proper region of interest (ROI). Using the tuneable option of CONRAD these ROI can now investigated in a much more efficient manner. Based on the Bragg edges (of different crystals) the attenuation spectra of these regions show enhanced contrast behaviour in the neighbourhood of proper wavelengths but not only in one point but all over the sample simultaneously. Recording radiographs at different (equidistant) wavelengths, one gets of each point of the sample the full information of attenuation. As a Bragg edge originates in the diffraction from a specific crystal lattice spacing of a material, lattice changes due to material stress can be imaged with this

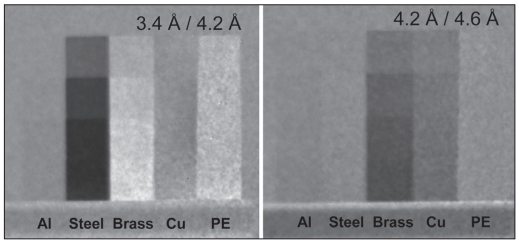

Fig. 3: Quotient images at wavelengths where the attenuation coefficients for Cu (left) and Fe (right) stay without change.

new method by mapping the shape, position and amplitude of a Bragg edge. In order to test this method a deformed steel plate of 5 mm thickness has been measured radiographically from 2.2 Å until 6.4 Å. in steps of 0.1 Å. The attenuation

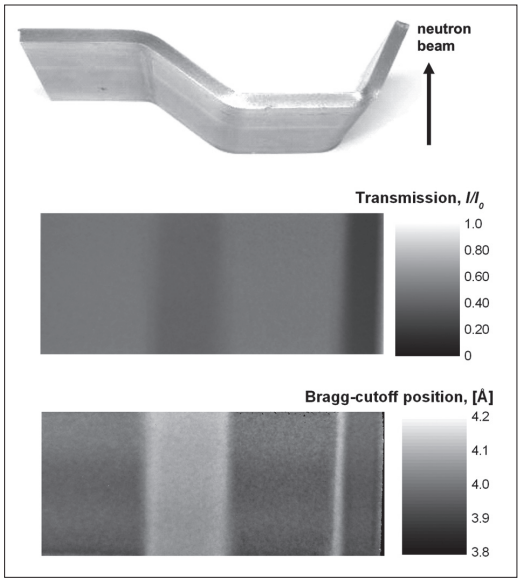

Fig. 4: Steel plate (50×10 mm^2) of 5 mm thickness was deformed – photo on the top. The radiography image is shown in the middle. 2D mapped position of the Bragg edge for each pixel in the deformed plate is shown in the bottom image. The obtained map can be related to the residual stress distribution in the plate.

spectrum (see Fig. 1b) for each point of the sample was derived and the resulted curve was fitted by a Gauss function. From the fit parameters the position of the Bragg edge was determined and a grey value was related to the obtained value. The results of the data evaluation are shown in Fig. 4. These promising results can be improved by decreasing the mosaic spread of the C–crystals and increase of energy resolution and hence the resolution of the Bragg edge scans. This would enable a fast spatial resolved stress mapping of big sample areas eventually to determine specific areas for more accurate diffraction investigations in dedicated stress and strain diffractometer.

[1] W. Treimer et al., Appl. Phys. Lett. **89**, 203504 (2006).

Corresponding author:
N. Kardjilov
kardjilov@hmi.de

Ion induced intermixing in thin metal tri-layers – a study with sub-nanometre depth resolution

N. Darowski[1], I. Zizak[1,2], A. Gupta[3], C. Meneghini[4], A. Erko[2]

■ 1 HMI, SF4 / SF2 ■ 2 BESSY, Berlin, Germany ■ 3 UGC-DAE Consortium for Scientific Research, Indore, India ■ 4 University of Rome, Rome, Italy

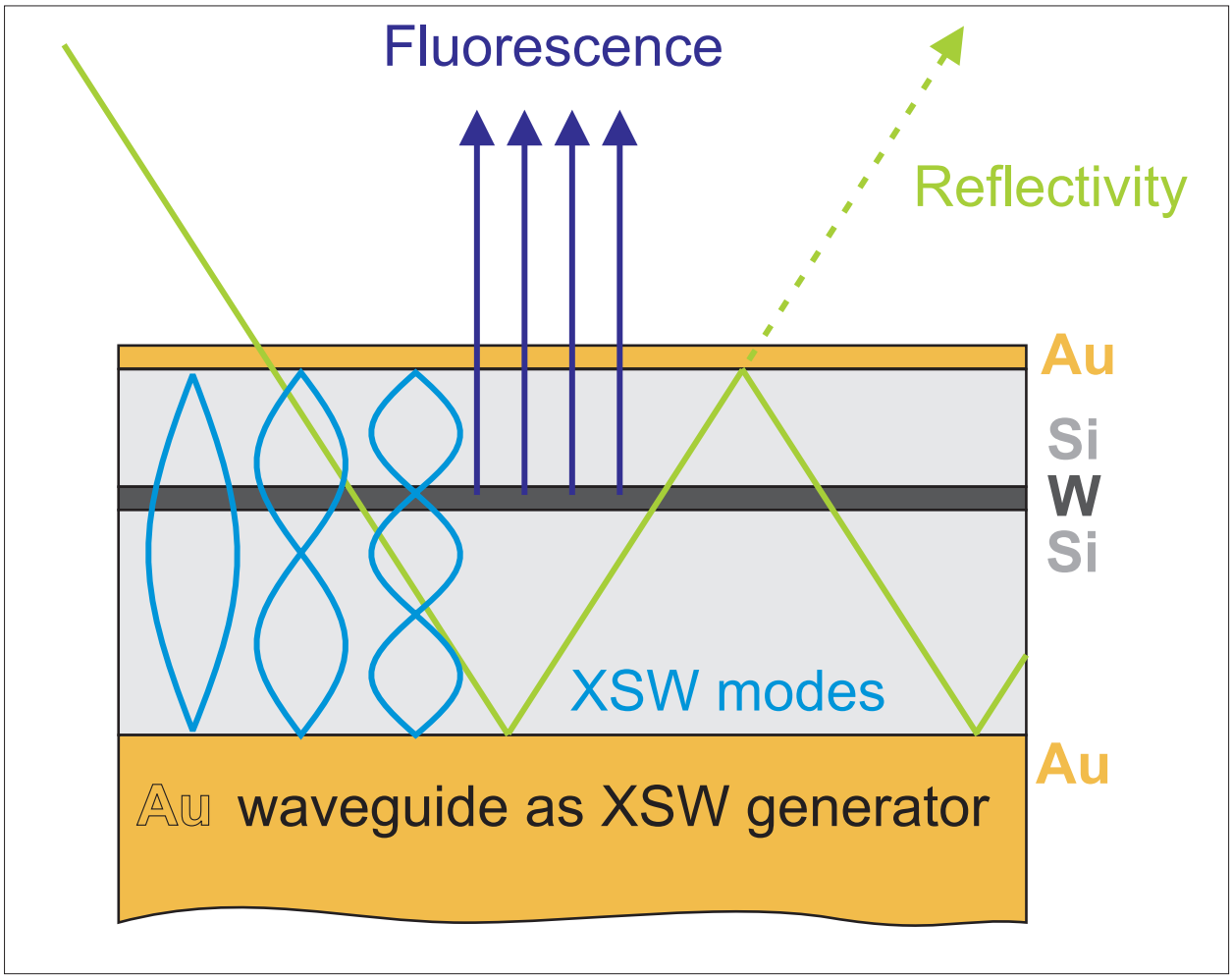

Fig. 1: Experiment geometry (See text for details)

Thin films and multilayers have emerged as important classes of nanostructured materials with immense possibilities of tailoring their properties in order to achieve the desired functionality. In multilay er structures, a particular property can get modified drastically as the thickness of the individual layers becomes comparable to the characteristic length scale of that given property, providing control over functionality through control of structure. Depending upon the application, layer thicknesses may vary from a fraction of a nanometre to few tens of nanometres. Since – in such multilayers – a large fraction of atoms resides at the surface/interfaces, the interfacial region plays a dominant role in determining their properties. Therefore, it is important to elucidate the interface

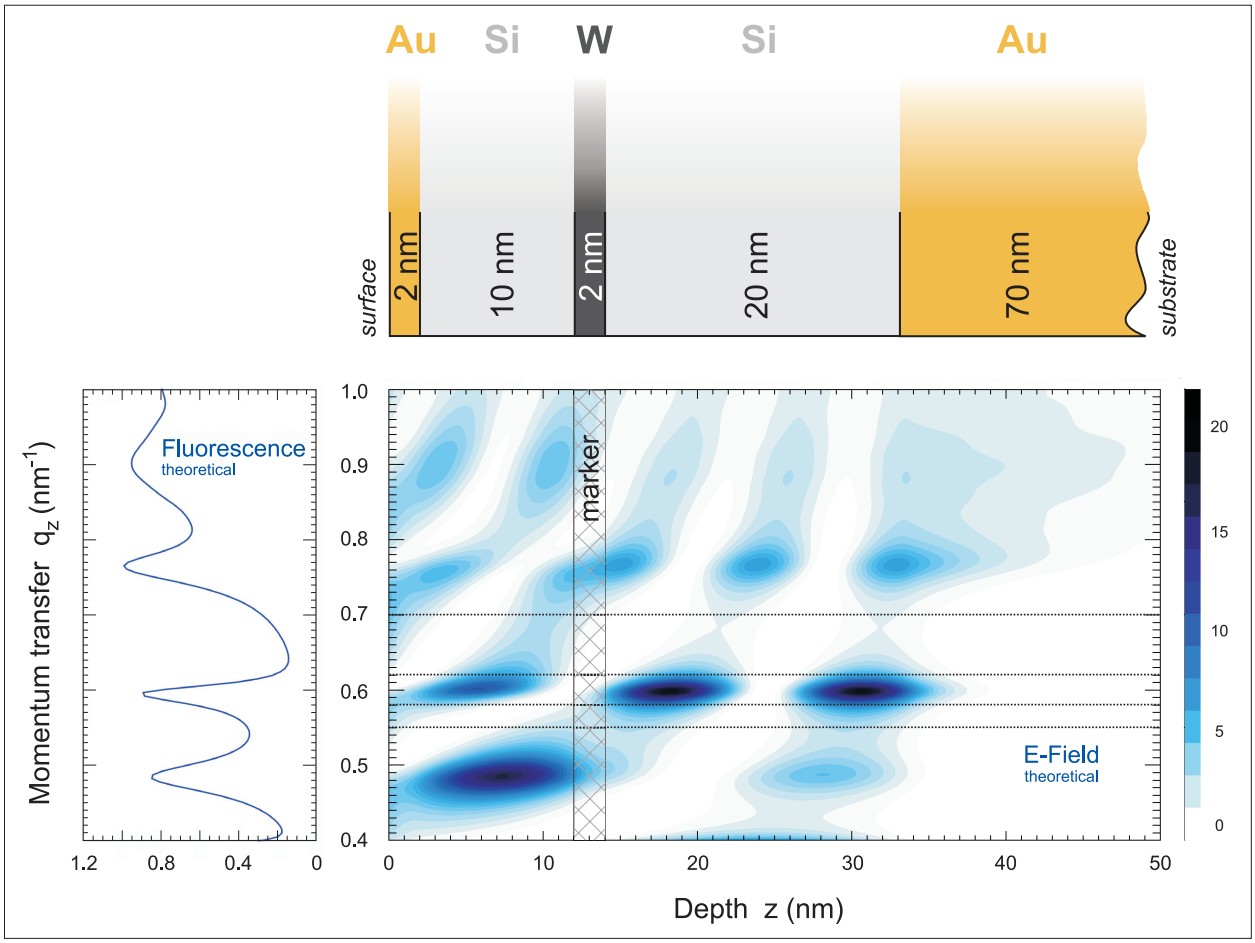

Fig. 2: Intensity distribution of the electrical wave field inside the sample versus the momentum transfer calculated at 10.3 keV (tungsten L-edge) together with the corresponding W fluorescence signal. Details of the multilayer structure are given in the upper part.

structure in order to understand their novel properties as well as to tailor the same via customized interface structures.

X-ray based characterization techniques are powerful tools for the study of atomic scale structure of materials. However, information obtained through x-ray diffraction techniques is usually averaged over the penetration depth of the probing x-rays, i.e., several microns for standard geometries. Depth selectivity can be obtained by generating x-ray standing waves (XSW) inside a layered structure by exploiting the effect of total reflection from an underlying layer composed of high Z material like Au [1]. Depth selectivity can be further enhanced when waveguide structures are used [2]. The geometry of the performed experiment is sketched in Fig. 1 together with the excitation modes of the x-ray standing wave.

Since the intensity of the x-rays is strongly localized in the region of antinodes, the standing wave field can be used as a localized probe with a sub-nanometer spatial resolution along the z-direction.

In case of a marker layer embedded into appropriate spacer layers, the fluorescence from the marker will depend upon the x-ray intensity at that point. As the angle of incidence of the probing x-rays with respect to the sample surface, θ, increases, the antinode position will move to larger depths. Whenever an antinode passes across the marker layer the corresponding fluorescence will exhibit a maximum as illustrated in Fig. 2. Thus, the q_z dependence of the fluorescence provides weighted information for a given element from different depth below the surface. The momentum transfer along z-direction is defined as $q_z = 4\pi \sin\theta / \lambda$, with λ denoting the wavelength of the probing x-rays.

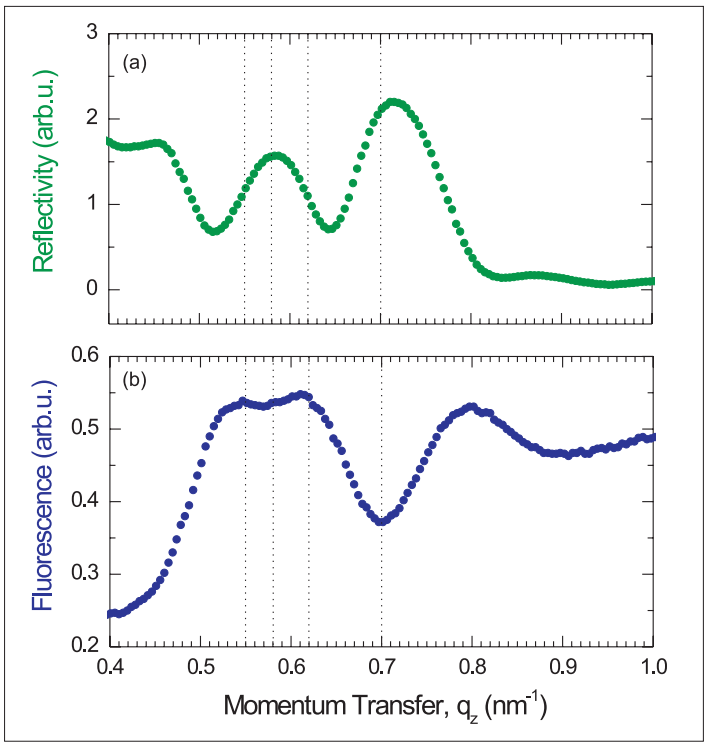

Fig. 3: Fluorescence and reflectivity intensity distribution recorded at 10.3 keV.

Here the capability of this technique is demonstrated in the study of swift heavy ion induced intermixing between a thin metal marker layer and silicon. Metal silicides are important for metallization applications in device production because of their low metal like resistivity, and high temperature stability and high electro-migration resistance. In this context, formation of metal silicides by heavy ion induced mixing has attracted considerable attention [3]. More recently, use of swift heavy ions for in-situ preparation of silicide thin films has been explored [4].

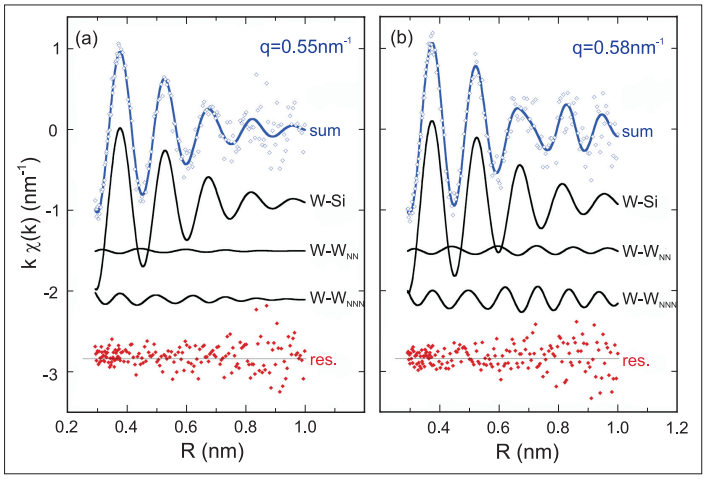

Fig. 4: XAFS data recorded at selected q_z together with considered fitting contributions.

The mechanism of energy transfer from the electronic system to atomic motion and subsequent intermixing is still not properly understood. Thus, a systematic study is needed in order to refine the model of ion-solid-interaction. Since intermixing can be as small as a nanometre or less, such studies require depths profiling techniques with a resolution of better than 1 nm. X-ray fluorescence measurements under standing wave conditions can provide the required depth resolution.
A waveguide structure was deposited on commercial Si substrate using magnetron sputtering. Details of the multilayer structure are given in Fig. 2. X-ray fluorescence patterns of the samples were recorded prior and after irradiation with 600 MeV Au ions from the ion beam laboratory ISL at the Hahn-Meitner-Institut Berlin. The bending magnet beamline KMC2 at the Berlin synchrotron radiation facility BESSY was used to set up the nanoprobe XAFS system. The x-ray beam in an energy range of 10 keV to 14 keV was monochromized by a double-graded-crystal monochromator and collimated in both directions using two slit systems and a collimating mirror. PIN diode detectors were utilized to measure both, the reflected beam and the fluorescence signal of the sample.

Fig. 3 shows the experimentally observed reflectivity (a) and tungsten L-edge fluorescence intensity (b) curves versus momentum transfer q_z recorded at 10.3 keV incidence energy. Maxima in fluorescence yield occur whenever an antinodal region of the XSW field coincides with the W marker layer. Different maxima correspond to different modes of the XSW. For the reflectivity signal, a reversed behaviour is expected and experimentally observed.

Fig. 4 shows tungsten L-edge data for two selected but only slightly different q_z together with the contributions which where taken into account for fitting. Even for only very small differences in, i.e., changes in information depth in the sub-nanometre range, significant changes in the XAFS signal and the fitting contributions were observed. The experimental data of the pristine sample as well as of the irradiated samples were fitted with a three-shell model: i) a W-Si shell, which is the main contribution to the whole XAFS signal, ii) a W-W shell similar to the W-W nearest neighbour distance in metallic W, and iii) a W-W shell which is similar to the W-W next nearest neighbour dis-

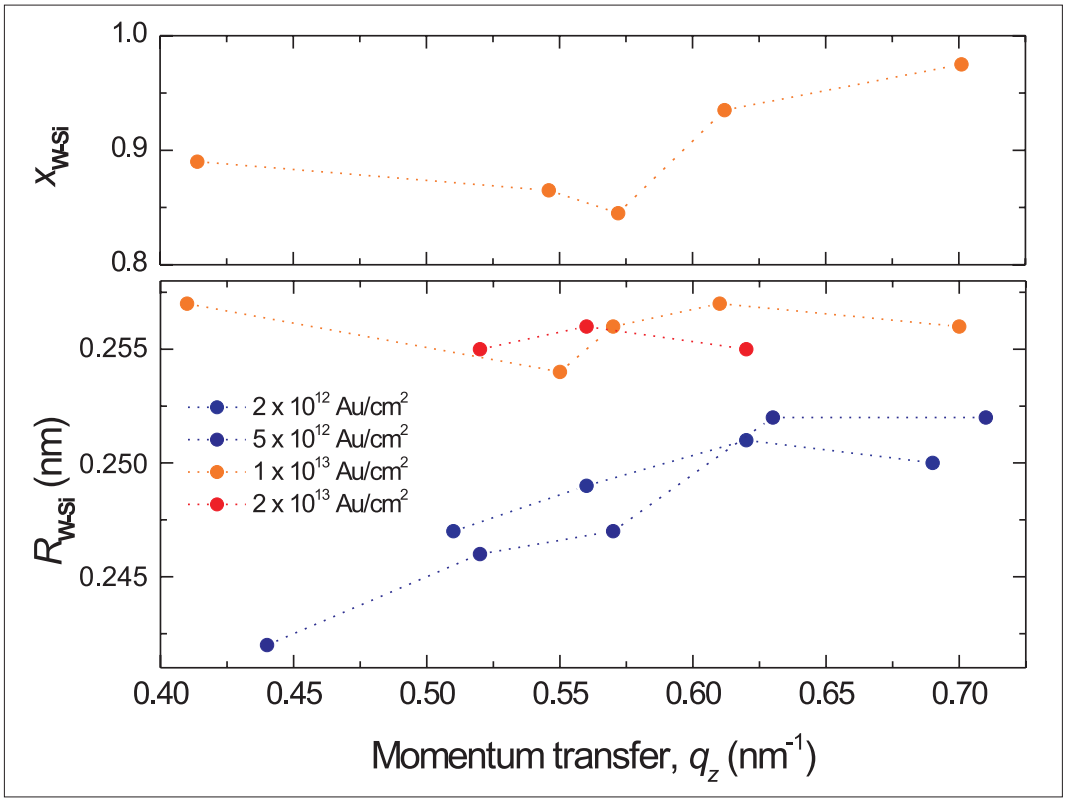

Fig. 5: Fluorescence and reflectivity intensity distribution recorded at 10.3 keV.

tance in metallic W. The XAFS data of the pristine sample suggest about 60% W in metallic environment and 40% in WSi_2. Irradiation provokes partial dissolution of W in Si giving rise to a higher fraction of W-Si correlation.

Fig. 5 shows the variation of fraction of W-Si bonds (a) and the W-Si bond length (b) as a function of q_z. A minimum of $x_{W\text{-}Si}$ is found at q_z=0.57nm^{-1}, i.e., at the position of the marker layer. $R_{W\text{-}Si}$ clearly depends on the irradiation fluence Φt. For $\Phi t \geq 1\times10^{13}$Au/cm^2 W-Si correlations dominate while metallic W contribution decreases. Φt is depth independent, indicating large intermixing. For $\Phi t \geq 1\times10^{13}$Au/cm^2 $R_{W\text{-}Si}$ is systematically shorter and increases with depth. A small $R_{W\text{-}Si}$ value is consistent with W-rich structures like W_5Si_3, whereas larger W-Si distances point to Si-rich WSi_2 phase. Depth resolved information about the various phases formed after irradiation are valuable for understanding the mechanisms of mixing, i.e., give insights into the interaction between high energetic ions and solid matter.

[1] S.K. Ghose, B.N. Dev, A. Gupta, Phys. Rev. B **64**, 233403 (2001)
[2] A. Gupta, R. Rajput, V.R. Reddy, M. Gupta, S. Bernstorff, H. Amenitsch, Phys. Rev. B **72**, 075436 (2005)
[3] R. Ayache, E. Richter, A. Bouabelleou, Nucl. Instrum. Methods B **216**, 137 (2004)
[4] P. Dhuri, A. Gupta, S.M. Chaudhari, D.M. Phase, D.K. Avasthi, Nucl. Instrum. Methods B **156**, 148 (1999)

Corresponding author:
N. Darowski
darowski@hmi.de

Element sensitive imaging of rodent and insect brains in 2D and 3D with neutrons and photons

M Kühbacher[1], B Grünewald[2], G Falkenberg[3], F Beckmann[4] and A Kyriakopoulos[1]
■ 1 HMI, SF6 ■ 2 Institut für Neurobiologie, Freie Universität Berlin, Berlin, Germany
■ 3 Hamburger Synchrotronstrahlungslabor HASYLAB at Deutsches Elektronen-Synchrotron DESY Hamburg, Germany ■ 4 GKSS-Research Center Geesthacht, Institute for Materials Research, Geesthacht, Germany

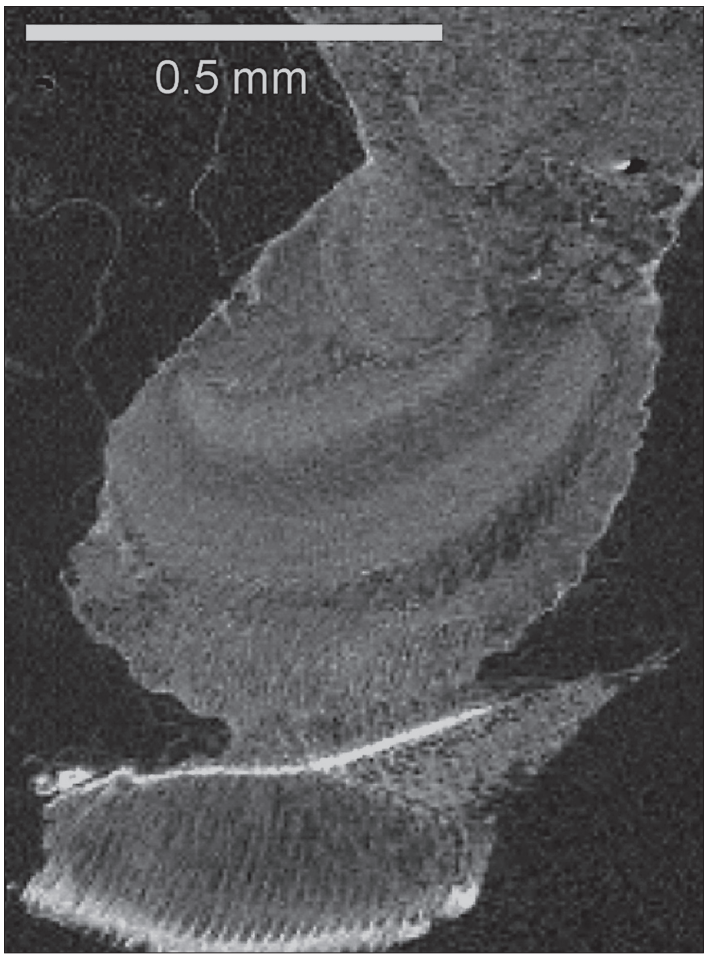

Fig. 1: Visualized section of a part of the brain of a honeybee after tomographic reconstruction.

The combination of radiotracers produced with neutrons at the reactor of the Hahn-Meitner-Institut and photons produced at HASYLAB and BESSY constitutes a powerful scientific toolkit for 2D and 3D chemical imaging of metal- and metalloid-containing proteins is in specific tissues - in particular in the central nervous system. In a series of experiments, this combination was used to allow new insights into the way nature solved complex structural and physiological chemical tasks.

In living organisms, metals and metalloids are involved in the production of free radicals – the causing factor for oxidative stress. However, metals and metalloids are also necessary components of specific antioxidant enzymes. The identification of metalloproteins, i.e. metal containing proteins, and the determination of their cellular and subcellular distribution will provide valuable hints with regard to the function and biological role of the metals and metalloids in question. Metalloproteomics, i.e. proteomics focused on metalloproteins, requires specific bioanalytical tools to identify these compounds and to study their distribution and biological functions.

A micro-synchrotron radiation X-ray fluorescence procedure (μ-SRXRF) was developed as such a bioanalytical tool. The procedure allows fast scanning of histological tissue sections with a focused X-ray beam and determination of the trace elements distributed among the brain areas by means of their characteristic X-ray emission. With new X-ray optics, a spatial resolution down to the micrometer range is achievable. The third spatial dimension of the elemental distribution pattern can be investigated by tomographic techniques. Microtomography using synchrotron radiation allows us to visualize the internal microscopic structure of small brains like the brain of the honeybee. While classical tomography provides a spatial resolution in the millimetre range, microtomography is expanding the spatial resolution down to a few micrometers. Beside other tomographic techniques based on absorption, phase-contrast, or X-ray scattering, X-ray fluorescence computed tomography achieves multielement capability by recording characteristic X-ray emission. The brains of diverse insects were investigated by

synchrotron radiation-based computered microtomography at BESSY and HASYLAB.

By labelling rats with radiotracers, the labelling techniques were optimized and the limit of detection improved to such an extent that even those labelled compounds present in the brain at very low concentrations could be detected. Fig. 3 shows the autoradiogram of a 10 µm thin brain-section of a rat radiolabelled with ^{73}As.

Fig. 2: Micro-tomographic data obtained by X-ray absorption tomography. The brain and the antennae of the honeybee head are visualized by segmentation.

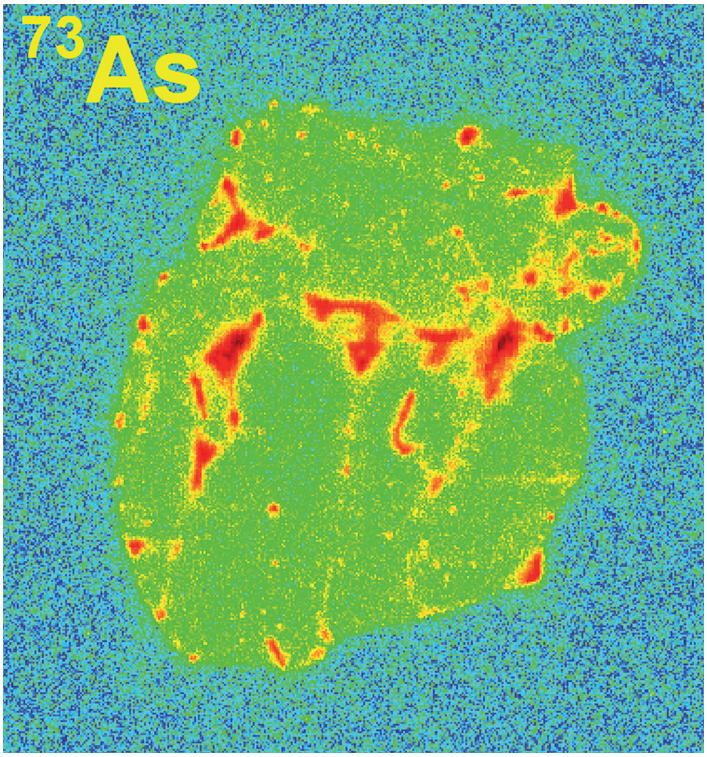

Fig. 3: Autoradiogram of ^{73}As in a 10 µm thin brain-section of a radiolabelled rat. The colours indicate the intensity of the radionuclide (red = high, blue = low).

Corresponding author:
M. Kühbacher
kuehbacher@hmi.de

Structure of the ^{10}Be nucleus: shell-model versus cluster structures

H. G. Bohlen[1], T. Dorsch[1,2], Tz. Kokalova[1], W. von Oertzen[1,3], Ch. Schulz[1], and C. Wheldon[1]
■ 1 HMI, SF7 ■ 2 TU München, Department E12 ■ 3 FU Berlin, Fachbereich Physik

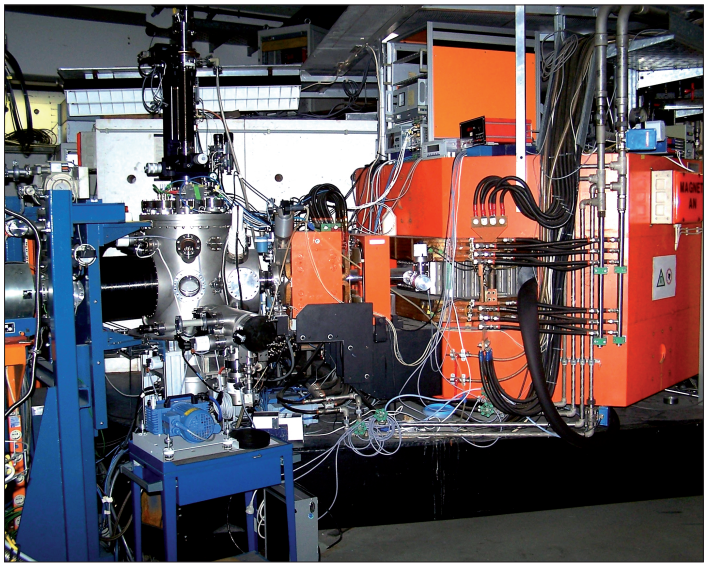

Fig. 1: The Q3D magnetic spectrograph at the HMI cyclotron. The quadrupole magnet and a small multipole magnet is seen in front of the first of three big dipoles (on the right). The beam line enters from the left into the cylindrical scattering chamber. From here the reaction products have to go a distance of 7.5 m to the focal plane, where they are detected.

In light nuclei, as for example Beryllium or Carbon isotopes, a competition exists between structures, (i) where all nucleons are bound in a central potential giving rise to shell-model states, or (ii) where α-clusters (^{4}He) with their high internal binding energy create a multi-centre structure. In the latter case even molecular states can be formed, i. e., for isotopes with neutron excess, where the exchange of the valence neutrons between the clusters gives rise to some extra binding energy. These effects are especially strong for states at excitation energies near the α-particle separation energy S_α [1], where an α-cluster is only weakly bound or is in a resonance state. In that case extra neutrons can be bound in molecular σ- and π-orbits for p-shell nuclei [2] with large distances between the clusters. Band structures result for such strongly deformed states. For a rotational band, which is built on a specific shell-model configuration, the maximum angular momentum is determined by the participating shell-model orbits. But higher angular momenta are possible for cluster or molecular structures, as has been shown by many theoretical calculations. In ^{10}Be such structures have been already identified some time ago [2].

We studied these structures of ^{10}Be at HMI's accelerator facility ISL using the ^{12}C(^{12}C,^{14}O)^{10}Be reaction at 211.4 MeV. The measurements were performed at the Q3D magnetic spectrograph (Fig. 1) at ISL. In Fig. 2 the excitation energy spectrum of ^{10}Be is plotted versus the scattering angle within the angular acceptance. Angular distributions were measured in this way for all the observed states in two angular sections (see the black and red data sets in Fig. 3). In this specifically chosen reaction the shape of the angular distributions is characteristic for the spin and parity of the states.

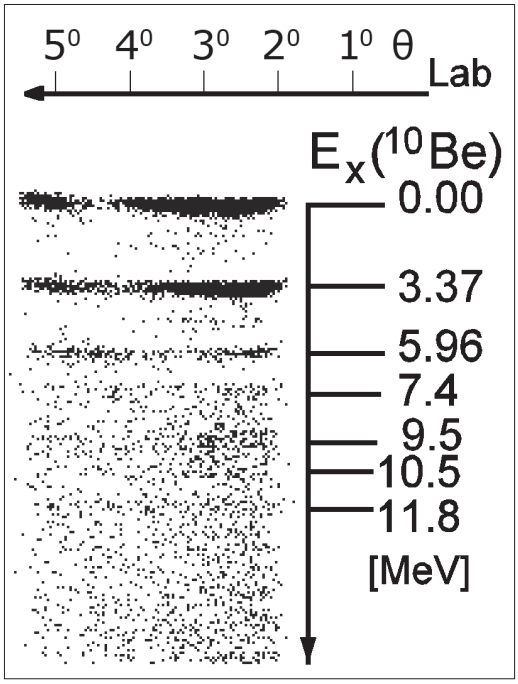

Fig. 2: Two-dimensional plot of the excitation energy E_x (in MeV)of ^{10}Be versus the scattering angle θ_{Lab} for out-going ^{14}O particles from the ^{12}C(^{12}C, ^{14}O)^{10}Be reaction. States of ^{10}Be up to 11.8 MeV excitation energy are observed.

Four bands have been identified in ^{10}Be (see Fig. 4). The structure information is deduced using the well known relation between angular momentum J and excitation energy E_x for members of a rotational band, where the inverse of the moment-of-inertia Θ of the rotating object enters as proportio-nality factor (these correspond to the slopes in Fig. 4). Information about the size and shape is deduced from the experimental value of Θ by comparing it to results from different models.

For the ground-state band (0^+_1, 2^+_1, 4^+) properties of the first two states can be described by shell-model (SM) calculations. However, a 4^+ member does not exist in the SM, whereas cluster models (CM) predict such a state at excitation energies in the range 10 – 13 MeV. In our measurement we identified this 4^+ state uniquely at E_x= 11.8(1) MeV by the shape of its angular distribution. This is in very good agreement with the CM-predictions. Detailed calculations within the cluster-model show a pronounced oblate shape. The second

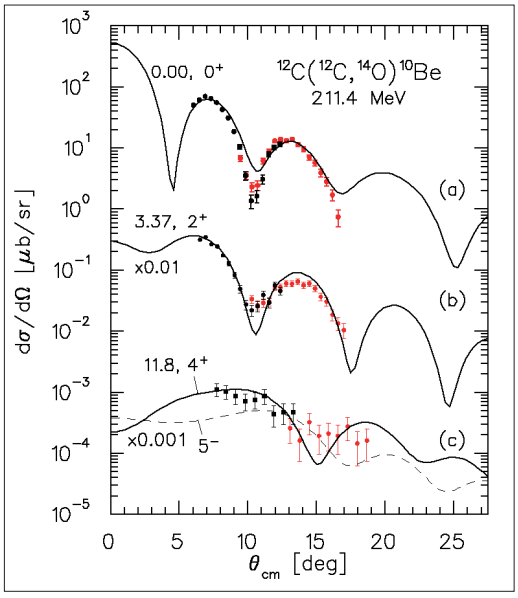

Fig. 3: Angular distributions of the 0^+, 2^+ and 4^+ states, which form the ground-state rotational band. The different shapes, especially at scattering angles below 15°, are characteristic for the spin and parity of corresponding states. Solid and dashed lines correspond to results from coupled-channels calculations.

band (K=2^+ in Fig. 4) has only two members, a 2^+_2 and a 3^+ state. The latter could be identified in our measurement by the decomposition of the angular distribution from the peak observed in Fig. 2 at 9.5 MeV. Both states have a large prolate deformation.

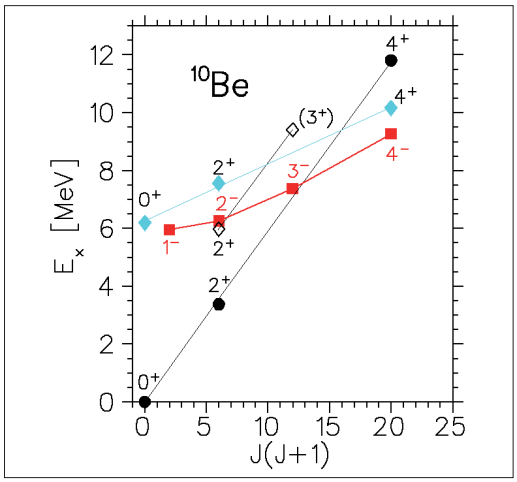

Fig. 4: Four different bands of ^{10}Be:
1. Ground state band (black dots)
2. K=2^+ band (open diamonds).
3. Molecular band (blue diamonds)
4. Odd-parity band (red squares)

The second 0^+ rotational band (0^+_2, 2^+_3, 4^+) built on the 0^+ state at 6.18 MeV. It is known to have a molecular structure: two α-particles at a mean distance of about 5.9 fm form a two-centre cluster system. The additional two neutrons of ^{10}Be are both in σ-orbits of the 1p-shell and stabilize the 2α-system as particle-stable structure. The 4^+ state of this band has also been uniquely identified recently [3] at 10.15 MeV. Such a *molecular* band does not exist in SM-calculations. The members of the odd-parity band (1^-, 2^-, 3^-, 4^-) are strongly populated in one-neutron transfer reactions on ^{9}Be$_{g.s.}$($3/2^-$). These states are described by the coupling of the $3/2^-$ core to a one-neutron configuration in the (sd)-shell. However, the excitation energies obtained from the SM are about 2 MeV too high (except for the 1^- state), whereas the CM describes these energies correctly with a σ- and a π-orbit for the neutrons.
Further information can be found in [4].

[1] K. Ikeda, Suppl. Prog. Theor. Phys. (Japan), Extra Number (1968).
[2] W. von Oertzen, Z. Physik A **357** (1997) 355.
[3] M. Freer et al., Phys. Rev. Lett. **96** (2006) 042501.
[4] H.G. Bohlen et al., Phys. Rev. C **75** (2007) 054604

Corresponding author:
H.-G. Bohlen
bohlen@hmi.de

The role of excited S multiplets in the magnetic relaxation of the high anisotropy barrier Mn_6 Single Molecule Magnet.

T. Guidi[1], O. Pieper[1,2], B. Lake[1,2], S. Carretta[3], P. Santini[3], G. Amoretti[3], J. Van Slageren[4], M. Russina[5], A. Buchsteiner[6], C.J. Milios[7], E.K. Brechin[7]

■ 1 HMI, SFN1 ■ 2 Technische Universität Berlin, Germany ■ 3 Dipartimento di Fisica, Universita' di Parma, Parma, Italy ■ 4 Physikalisches Institut, Universität Stuttgart, Stuttgart, Germany ■ 5 HMI SF1 ■ 6 HMI SF2 ■ 7 School of Chemistry, University of Edinburgh, Edinburgh, UK

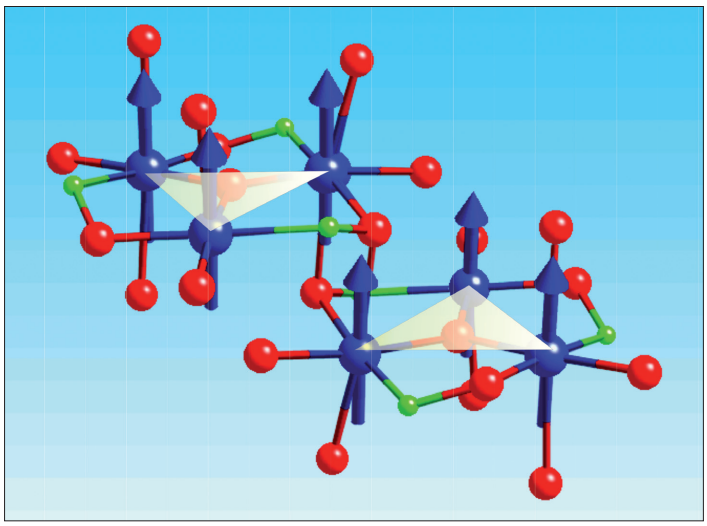

Fig. 1: Structure of the Mn_6-(Et $saoH_2$) molecular core. The Mn(III) ions are located at the vertices of two oxo-centered triangles. Color scheme: Mn, blue, O, red, N, green. H and C ions are omitted for clarity.

The present technology for data storage devices is dominated by magnetic hard disk drives. During the last decades, the ever-increasing demand for high performing, light and reduced-sized devices has driven the exponential increase of areal density storage. This behaviour is foreseen to end when the so called 'superparamagnetic limit' is reached. The continuous shrinking of the volume of the magnetic particles, which store one bit of information, is limited. When the magnetic energy stored in one grain, which is proportional to the volume of the particle, is comparable to the thermal energy, the magnetization M will freely fluctuate resulting in a loss of information. Therefore new concepts and systems are needed to provide a solution for the next generation of technology.

Single Molecule Magnets (SMM) are promising systems for the realisation of ultra-fast/ultra-high density classical bits. They are clusters consisting of a small number of transition metals ions, exchange coupled via organic ligands and arranged in a crystal lattice with a negligible interaction between different magnetic units. The dominant exchange interactions between the spins of the ions give rise to a high-spin ground state S associated with the cluster. At the same time, the presence of a large easy-axis magneto-anisotropy determines the Zero-Field Splitting (ZFS) of the S state sublevels, with an energy barrier that separates the "spin-up" (S_z=S) and "spin-down" (S_z=–S) states, of height given by U~|D|S^2 (where D is the axial anisotropy parameter). These systems thus represent a bottom-up approach to nanoscale magnetism. The main focus of the research in this field is to find the right ingredients for the synthesis of systems with high enough anisotropy to hinder thermal fluctuations, and allow storage of a bit of information in just one single molecule.

Considerable effort has been devoted to increasing the barrier height and thus making technological applications feasible at temperatures higher than the cryogenic range. Up to now, the maximum height for the anisotropy barrier (about 74 K) has been obtained for the Mn_{12} cluster [1].

Recently, a new series of Mn_6 clusters of generic formula $[Mn_6O_2(oxime)_6(carboxylate)_2(EtOH)_n(H_2O)_m](EtOH)_y$, displaying a SMM behaviour has been synthesized.

The magnetic core consists of six Mn(III) (s=2) ions arranged into two $\{Mn_3(\mu_3\text{-}O)\}$ triangular subunits bridged together by two oximato oxygen atoms (Fig. 1). By changing the nature and the arrangement of ligands, a series of compounds with different Mn-Mn exchange couplings and total spin ground state S has been obtained.

In particular, the $[Mn_6O_2(Et\text{-}sao)_6(O_2CPh)_2(EtOH)_4(H_2O)_2]\cdot{}_2EtOH$ (**2**·2EtOH) compound (briefly Mn_6-(Et $saoH_2$)) has a high-spin S=12 ground state due to the dominant intra- and inter-triangle ferromagnetic (FM) interactions. A preliminary fit of the magnetization data indicates an axial ZFS parameter D=–0.62 K, leading to an upper-limit estimate for the anisotropy barrier of U=|D| S^2≈89K, the highest so far. However, a much

smaller value for the experimental effective anisotropy barrier U_{eff} (~53 K) has been deduced from relaxation data [2]. This large discrepancy has been tentatively attributed to the presence of low-lying excited states, which could play a role in the relaxation dynamics and lower the energy barrier for the reversal of M.

To shed light on this issue, an accurate determination of the low-energy eigenstates and eigenvalues is required. Hence, we have used the NEAT time of flight spectrometer to investigate the spin dynamics of the Mn_6-(Et $saoH_2$).

By measuring with an incident wavelength of 4.6 and 5 Å, we have directly observed the inter-multiplet transitions from the S=12 ground state to the low-lying S=11 excited spin states (Fig. 2). These measurements provide essential information to determine the intra- and inter-triangles exchange parameters and the single-ion anisotropies. In particular, we have found that there are many excited multiplets (with S<12) partially nested within the S=12 ground state multiplet (see Fig. 3). This nesting leads to a very large degree of S mixing [3] of the spin wavefunctions and strongly influences the relaxation behavior. In fact, several inter-multiplet relaxation paths, via a combination of multi-step Orbach and tunneling processes, contribute to the decay of the molecular magnetization. This leads to a large reduction of the effective energy barrier.

To model this system the full spin Hilbert space has to be included in the calculations and all the main local crystal-field (CF) parameters (at least three for each inequivalent Mn ion) have to be considered. Preliminary fits of the neutron cross section are shown in Fig. 2, which account very well for the main features of the low-resolution spectra.

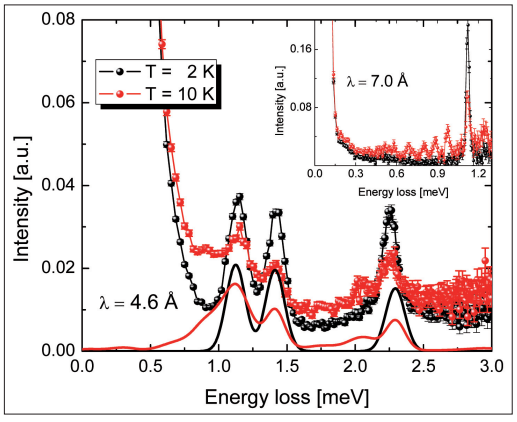

Fig. 2: Inelastic neutron spectra of Mn_6-(Et $saoH_2$) sample collected on NEAT time-of-flight spectrometer using an incident wavelength of 4.6 Å and 7 Å (inset) for two different temperatures, 2 K (black) and 10 K (red). The continuous lines represent the spectra calculated with the best fit exchange and anisotropy parameters.

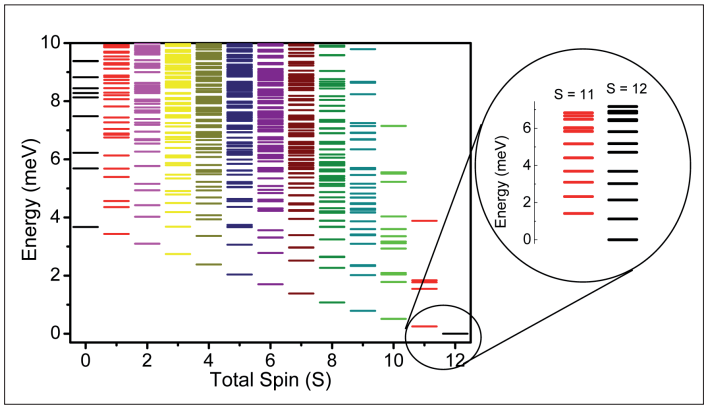

Fig. 3: Eigenvalues of the isotropic part of the Hamiltonian as a function of the total spin quantum number S. The magnification shows the anisotropy energy level splitting of the two lowest energy S states evidencing the nesting of excited states within the S=12 ground multiplet.

To investigate in detail the anisotropic part of the Hamiltonian, we have performed high-resolution measurements at = 7Å and at two different temperatures, 2 and 10 K. Several excitations within the ground S=12 multiplet and within the lowest excited S=11 multiplet (Fig. 2, inset) have been observed, confirming the nesting of the lowest excited S multiplets within the ground one. Theoretical work is in progress to definitely fix the CF parameters.

Recently, a chemical engineering of the material by further changing the ligands has resulted in the synthesis of an analog Mn_6 compound, Mn_6O_2(Et-sao)$_6$ $(O_2CPh(Me)_2)_2(EtOH)_6$) [4], with a stronger FM exchange and hence higher-lying excited spin multiplets. This reduces their role in magnetic relaxation and substantially increases the effective barrier to U_{eff} = 86.4 K. This new Mn_6 compound has to date the highest effective barrier of any SMM, including Mn_{12}.

[1] Sessoli, R.; Gatteschi, D.; Caneschi, A.; Novak, M. A. Nature 1993, **365**, 141; N.E. Chakov, J. Lee, A. G. Harter, S. O. Hill, N. S. Dalal, W. Wernsdorfer, K. A. Abboud and G. J. Christou,J. Am. Chem. Soc., **128**, 6975 (2006)

[2] Milios, C. J.; Vinslava, A.; Wood, P. A.; Parsons, S.; Wernsdorfer, W.; Christou, G.; Perlepes, S. P.; Brechin, E. K. J. Am. Chem. Soc. 2007, **129**, 8.

[3] S. Carretta, P. Santini, G. Amoretti, T. Guidi, J. R. Copley, Y. Qiu, R. Caciuffo, G. Timco, and R. E. Winpenny, Phys. Rev. Lett. **98**, 167401 (2007).

[4] C. J. Milios, A. Vinslava, W. Wernsdorfer, S. Maggach, S. Parson, S. P. Perlepes, G. Christou, E. K. Brechin, J. Am. Chem. Soc. **129**, 2754, (2007).

Corresponding author:
T. Guidi
tatiana.guidi@hmi.de